

## A CLOSE RELATIONSHIP BETWEEN Ly $\alpha$ AND Mg II IN GREEN PEA GALAXIES<sup>\*†</sup>

ALAINA HENRY<sup>1,2</sup>, DANIELLE A. BERG<sup>3</sup>, CLAUDIA SCARLATA<sup>4</sup>, ANNE VERHAMME<sup>5</sup>, DAWN ERB<sup>3</sup>

*Draft version March 29, 2018*

### ABSTRACT

The Mg II  $\lambda\lambda 2796, 2803$  doublet is often used to measure interstellar medium absorption in galaxies, thereby serving as a diagnostic for feedback and outflows. However, the interpretation of Mg II remains confusing, due to resonant trapping and re-emission of the photons, analogous to Ly $\alpha$ . Therefore, in this paper, we present new MMT Blue Channel Spectrograph observations of Mg II for a sample of 10 Green Pea galaxies at  $z \sim 0.2 - 0.3$ , where Ly $\alpha$  was previously observed with the Cosmic Origins Spectrograph on *Hubble Space Telescope*. With strong, (mostly) double-peaked Ly $\alpha$  profiles, these galaxies allow us to observe Mg II in the limit of low H I column density. We find strong Mg II emission and little-to-no absorption. We use photoionization models to show that nebular Mg II from H II regions is non-negligible, and the ratios of Mg II  $\lambda\lambda 2796, 2803$ /[O III]  $\lambda 5007$  vs. [O III]  $\lambda 5007$ /[O II]  $\lambda 3727$  form a tight sequence. Using this relation, we predict intrinsic Mg II flux, and show that Mg II escape fractions range from 0 to 0.9. We find that the Mg II escape fraction correlates tightly with the Ly $\alpha$  escape fraction, and the Mg II line profiles show evidence for broader and more redshifted emission when the escape fractions are low. These trends are expected if the escape fractions and velocity profiles of Ly $\alpha$  and Mg II are shaped by resonant scattering in the same low column density gas. As a consequence of a close relation with Ly $\alpha$ , Mg II may serve as a useful diagnostic in the epoch of reionization, where Ly $\alpha$  and Lyman continuum photons are not easily observed.

### 1. INTRODUCTION

In the spectra of star-forming galaxies, interstellar and circumgalactic medium (ISM and CGM) absorption in the Mg II  $\lambda\lambda 2796, 2803$  doublet has been used to study galactic outflows (Weiner et al. 2009; Rubin et al. 2010, 2011; Coil et al. 2011; Erb et al. 2012; Martin et al. 2012; Kornei et al. 2012; Tang et al. 2014; Zhu et al. 2015; Bordoloi et al. 2016; Finley et al. 2017). At  $z \sim 1$ , alongside a complex of near ultraviolet (NUV) Fe II lines, the Mg II lines are redshifted into the rest-frame optical where they are readily observed from the ground. Consequently, as a diagnostic, Mg II plays an important role for measuring the evolution of galactic outflows, feedback, and the CGM.

Despite its potential usefulness, most studies acknowledge that, as a resonance feature, the Mg II  $\lambda\lambda 2796, 2803$  doublet can be complicated to interpret. The lines are commonly observed with P-Cygni profiles, showing blueshifted absorption and redshifted emission. This line

shape is produced when the absorbed photons scatter in a moving envelope of gas. The detection of P-Cygni emission implies that the pure absorption profile has been “filled in” by re-emission of absorbed photons. Hence, absorption-line measurements of outflow velocity, column density, and line saturation can be incorrect (Prochaska et al. 2011; Scarlata & Panagia 2015). Nevertheless, the Mg II  $\lambda\lambda 2796, 2803$  doublet lines are strong, giving sensitivity to low column densities of gas. Modeling of the expanding medium generating the P-Cygni profile can also constrain the geometry, velocity, and density of absorbing and emitting gas (Prochaska et al. 2011; Scarlata & Panagia 2015; Zhu et al. 2015, Carr et al., submitted), thereby providing measurements of mass outflow rates. Therefore, including Mg II alongside other UV lines can be useful as we aim to leverage all available information to understand outflows and the CGM. However, these features *must* be interpreted carefully.

The interpretation of Mg II  $\lambda\lambda 2796, 2803$  is further complicated by a possible contribution from nebular emission. Both Erb et al. (2012) and Jaskot & Ravindranath (2016) point out that photoionization models predict appreciable Mg II  $\lambda\lambda 2796, 2803$  emission from H II regions. While this emission is erased by absorption in most cases, Erb et al. argue that it may account for the differences in the observed profiles of Mg II and Fe II in galaxies at  $z \sim 2$ . Remarkably, nebular Mg II has been detected from some regions of Orion (Boeshaar et al. 1982), and in some SDSS spectra of galaxies at  $z > 0.36$  (Guseva et al. 2013). Recently, Izotov et al. (2018) report Mg II emission from a low-redshift Lyman Continuum leaker, and Finley et al. (2017) observe that Mg II profiles transition from absorption to pure emission in  $z \sim 1$  galaxies with  $M \lesssim 10^9 M_{\odot}$ . Mg II emission is even seen in the supernova Refsdal host galaxy (Karman et al. 2016).

<sup>1</sup> Space Telescope Science Institute, 3700 San Martin Drive, Baltimore, MD, 21218, USA ahenry@stsci.edu

<sup>2</sup> Department of Physics & Astronomy, Johns Hopkins University, Baltimore, MD 21218, USA

<sup>3</sup> Center for Gravitation, Cosmology, and Astrophysics, Department of Physics, University of Wisconsin Milwaukee, 3135 Maryland Ave, Milwaukee, WI 53211, USA

<sup>4</sup> Minnesota Institute for Astrophysics, School of Physics and Astronomy, University of Minnesota, 316 Church Str. SE, Minneapolis, MN 55455, USA

<sup>5</sup> Observatoire de Genève, Université de Genève, 51 Ch. des Maillettes, 1290 Versoix, Switzerland

<sup>\*</sup> Based on observations made with the NASA/ESA Hubble Space Telescope, which is operated by the Association of Universities for Research in Astronomy, Inc., under NASA contract NAS 5-26555. These observations are associated with program 12928, 11727, 13744, and 14201.

<sup>†</sup> Observations reported here were obtained at the MMT Observatory, a joint facility of the Smithsonian Institution and the University of Arizona.

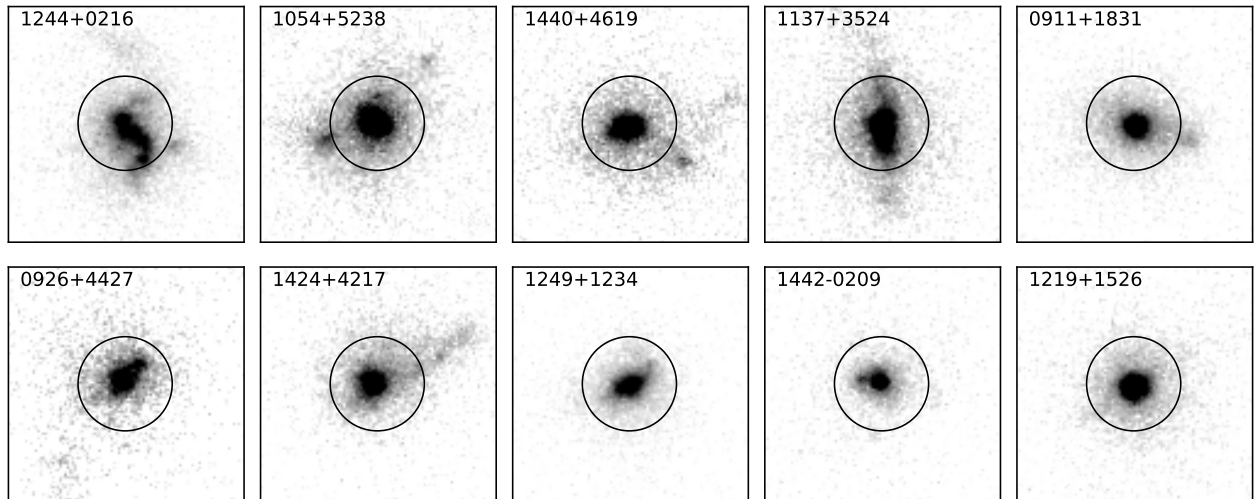


**Figure 1.** Cutouts from the COS target acquisition images show the UV continuum light from the Green Pea galaxies in this sample. Stamps are  $2.5''$  on a side, similar to the diameter of the full COS aperture. The circle marks the  $1''$  diameter portion of the COS aperture that is unvignetted.

Importantly, the production of nebular line photons, and subsequent resonant scattering in neutral/low ionization state gas is identical to the Ly $\alpha$  line. In fact, some observations have suggested that we may find similarities between these two features. First, studies of galaxies at  $z \sim 1 - 2$  have reported that Mg II emission is more common in galaxies with lower masses, higher specific star-formation rates, and blue colors (Weiner et al. 2009; Erb et al. 2012; Kornei et al. 2013; Finley et al. 2017). These are the same properties that appear to favor Ly $\alpha$  emission from galaxies (Gawiser et al. 2007; Finkelstein et al. 2007; Henry et al. 2015). Second, spatially extended Mg II has been detected in two intermediate redshift galaxies (Rubin et al. 2011; Martin et al. 2013), analogous to the ubiquitous Ly $\alpha$  halos seen at both low and high redshifts (Hayes et al. 2014; Wisotzki et al. 2016; Leclercq et al. 2017). Nevertheless, in the only study that has compared Ly $\alpha$  and Mg II to date, Rigby et al. (2014) find no correlations for a sample of five galaxies.

For most redshifts, the wavelengths of Mg II and Ly $\alpha$  have made comparison between the lines difficult. Consequently, more questions than answers remain about the interpretation of Mg II, its similarities or differences with Ly $\alpha$  and other ISM absorption lines, and its ability to serve as a diagnostic for outflows. To address these issues, in this paper we present the first observations of Mg II from  $z \sim 0.2 - 0.3$  Green Pea galaxies. With existing high-resolution, high signal-to-noise Ly $\alpha$  and far ultraviolet (FUV) ISM absorption line spectra (Henry et al. 2015), we are able to compare the Mg II to other widely-used diagnostics. This sample allows us to explore Mg II in the limit of low H I column density that has been inferred from Ly $\alpha$  profiles (Henry et al. 2015) and, in some cases, Lyman Continuum (LyC) leakage (Izotov et al. 2016a,b, 2017, 2018). By focusing on this select set of rare, nearby galaxies, we can aim to better understand Mg II under physical conditions that may be common at high-redshifts. Ultimately, as we will demonstrate, Mg II observations of these galaxies form a strong motivation

for increased samples, covering a greater dynamic range of galaxy properties.

This paper is organized as follows. In §2 we present our sample, observations, and data reduction. In §3 we show that the Green Pea galaxies have consistent strong Mg II  $\lambda\lambda 2796, 2803$  emission and almost no absorption. We present measurements of these emission lines, and predictions for intrinsic Mg II strength using Cloudy photoionization models (Ferland et al. 2017). Using this intrinsic Mg II prediction, we calculate Mg II escape fractions, analogous to Ly $\alpha$  escape fractions. In §4 we explore how the Mg II escape fraction, equivalent width, and line velocity structure vary due to radiation transport effects, showing that Mg II escape fractions form a tight sequence with Ly $\alpha$  escape fractions. Finally, §5 summarizes these results and discusses their implications, considering the utility of Mg II as a diagnostic in the epoch of reionization. Throughout this paper, we adopt a convention where positive equivalent widths refer to emission, while negative equivalent widths indicate absorption.

## 2. SAMPLE, OBSERVATIONS, AND DATA

Green Peas are a sample of  $z \sim 0.2$  galaxies with extremely high-equivalent width emission lines (Cardamone et al. 2009), making them compelling analogs for high-redshift objects. We have selected ten such galaxies for observations in the Mg II  $\lambda\lambda 2796, 2803$  doublet, using two main criteria. First, we require that the objects have existing observations of Ly $\alpha$  and UV continuum from the Cosmic Origins Spectrograph (COS) on the *Hubble Space Telescope*, with sufficient sensitivity to measure metal absorption lines. Second, we chose objects with  $z > 0.18$ , placing Mg II  $\lambda\lambda 2796, 2803$  at observed wavelengths greater than  $3300 \text{ \AA}$ . We chose eight of the ten galaxies from the Green Peas presented in Henry et al. (2015), adding one galaxy from Yang et al. (2017; HST GO 14201), and a LyC leaker from Izotov et al. (2016; HST GO 13744). All of the supplemental COS observations use the high-resolution G130M and/or G160M gratings. The sample is listed in Table 1. Figure 1 shows their COS NUV target acquisition images.

**Table 1**  
Green Pea Sample

ID	RA (J2000)	DEC (J2000)	$z^a$	$E(B-V)_{MW}^b$ (mag)	Exposure Time <sup>c</sup> (seconds)	SDSS $u$ (mag)	Slit Loss Correction <sup>d</sup>	COS Gratings <sup>e</sup>
0911+1831	09 11 13.34	18 31 08.2	0.26224	0.025	$4 \times 1800$	19.8	2.0	G130M, G160M
0926+4427	09 26 00.44	44 27 36.5	0.18070	0.017	$4 \times 1800$	19.2	2.4	G130M, G160M
1054+5238	10 53 30.80	52 37 52.9	0.25265	0.013	$3 \times 1800$	19.0	2.0	G130M, G160M
1137+3524	11 37 22.14	35 24 26.7	0.19440	0.016	$3 \times 900$	19.1	1.5	G130M, G160M
1219+1526	12 19 03.98	15 26 08.5	0.19561	0.024	$4 \times 1800$	19.8	1.9	G130M, G160M
1244+0216	12 44 23.37	02 15 40.4	0.23942	0.021	$3 \times 1800$	19.6	2.1	G130M, G160M
1249+1234	12 48 34.63	12 34 02.9	0.26340	0.025	$4 \times 1800$	20.2	1.4	G130M, G160M
1424+4217	14 24 05.72	42 16 46.3	0.18480	0.009	$3 \times 2000$	19.3	1.6	G130M
1440+4619	14 40 09.94	46 19 36.9	0.30076	0.012	$3 \times 600$	19.8	1.8	G160M
1442-0209 <sup>f</sup>	14 42 31.37	-02 09 52.8	0.29367	0.047	$3 \times 1800$	21.5	2.9	G160M

<sup>a</sup> The redshifts are determined from SDSS spectra, which have uncertainties of order a few  $\text{km s}^{-1}$ .

<sup>b</sup> The Milky Way extinction values are from Schlafly & Finkbeiner (2011), acquired from the NASA Extragalactic Database. We use the Fitzpatrick (1999) extinction curve to correct the UV spectra for foreground attenuation.

<sup>c</sup> An exposure time specified, for example, as  $3 \times 1800$  implies that three 1800 second exposures were combined.

<sup>d</sup> The slit loss correction is estimated by calculating the SDSS  $u$ -band magnitude directly from each spectrum, and comparing this result to the imaged SDSS  $u$ -band magnitude.

<sup>e</sup> The COS gratings used for comparison in this paper; low resolution gratings were not considered.

<sup>f</sup> This Green Pea galaxy was drawn from the Izotov et al. (2016b) sample of Lyman Continuum leakers.

We observed these ten galaxies using the Blue Channel Spectrograph (Angel et al. 1979) at the MMT on 28-29 March 2017. A  $1''$  slit was used with the 832 lines  $\text{mm}^{-1}$  grating at second order, achieving a spectral resolution of  $90 \text{ km s}^{-1}$ . The central wavelength of  $3605 \text{ \AA}$  provided wavelength coverage from 3150 to  $4090 \text{ \AA}$  in the observed frame. Total exposure times were chosen to obtain an estimated continuum signal-to-noise (SNR) of ten per spectral resolution element, and were divided into three or four exposures per object. Since atmospheric dispersion is significant at these wavelengths (Filippenko 1982), we ensured that the observations were carried out at the lowest possible airmasses (less than 1.25, except for 1442-0209 which reached 1.36). We also reset the slit position angle for each exposure, choosing the parallactic angle midway through the exposure. Likewise, because the Blue Channel Spectrograph does not compensate for flexure, arc lamp exposures were taken before the observation of each object. Finally, we note that observing conditions were non-photometric, with light cirrus and variable seeing around  $1''$ .

The spectra were processed using ISPEC2D (Moustakas & Kennicutt 2006), a long-slit spectroscopy data reduction package written in IDL, and then extracted and calibrated using standard IRAF procedures. A master bias frame was created from 10 zero-second exposures by discarding the highest and lowest value at each pixel and taking the median. Master sky and dome flats were similarly constructed after normalizing the counts in the individual images. Those calibration files were then used to bias-subtract, flat-field, and illumination-correct the raw data frames. Due to faint continuum in individual exposures, the multiple sub-exposures of each target were median combined prior to extraction, also eliminating cosmic rays in the process. Extraction of the one-dimensional spectra was performed using a box-car aperture capturing 99% of the light in the Mg II feature and a median sky subtraction along each column of the dispersion direction. For each object, the wavelength calibration was applied from the HeArHgCd comparison lamps taken at the same telescope pointing. A sensitivity

curve was derived from several standard stars observed during twilight, and used to flux calibrate the individual 1D spectra. This spectrophotometric data reached  $3200 \text{ \AA}$ , so although our Blue Channel spectra reached  $3150 \text{ \AA}$ , we do not consider these wavelengths in any analysis. Finally, the spectra were corrected to a heliocentric velocity reference frame, using IRAF's *rvcorrect* procedure.

Since we aim to measure Doppler shifts for the Mg II lines, we tested the accuracy of our wavelength calibration. For this check, we compared our data to the night sky spectrum from Hauschik 2003, taken with the Ultraviolet and Visible Echelle Spectrograph (UVES) on the Very Large Telescope (VLT). This spectrum has an average wavelength accuracy of  $17 \text{ m\AA}$  ( $1.5 \text{ km s}^{-1}$  at  $3400 \text{ \AA}$ ). First, we downgraded this high resolution spectrum to  $90 \text{ km s}^{-1}$ , and rebinned it to match the Blue Channel data. Then we cross-correlated the spectra in  $200 \text{ \AA}$  segments to derive any residual velocity shifts between the UVES and Blue Channel data. We find that, for some wavelengths, the VLT and MMT sky spectra show substantial time, airmass and/or site-dependent variations that limit the utility of this method. Nevertheless, at wavelengths where the spectra appear to have a similar spectral-morphology, this test indicates that the calibration in our data is accurate to  $20 \text{ km s}^{-1}$ .

In order to compare the MMT spectra with SDSS and COS observations, we calculate slit-loss corrections to place the Blue Channel spectra on an absolute flux scale. We convolve each spectrum with the SDSS  $u$ -band throughput ( $\lambda_{center} \sim 3600 \text{ \AA}$ ,  $\text{FWHM} \sim 500 \text{ \AA}$ ), calculating a synthetic  $u$ -band magnitude for the Blue Channel data. Comparing to the SDSS photometry, we find that a factor of around two is required to correct for slit-losses and non-photometric conditions. The SDSS  $u$ -band magnitudes and slit-loss corrections are given in Table 1, and are applied to the Mg II fluxes in §3. Although we do not detect Mg II emission extending beyond the continuum, we acknowledge that these corrections could still be lower limits for the lines, if extended, low surface brightness line emission is missed by our observations.

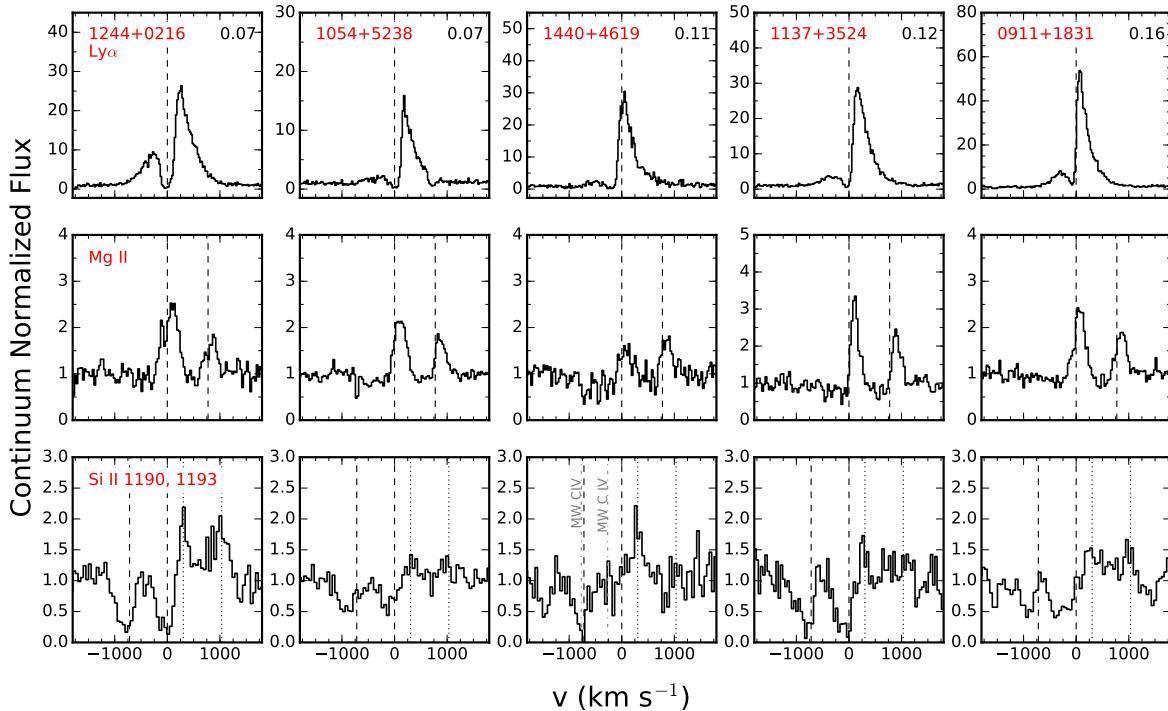


**Figure 2.** The Mg II  $\lambda\lambda 2796, 2803$  lines are compared to Ly $\alpha$  and Si II, plotted with respect to the systemic redshift at  $v = 0$ . The top panels show Ly $\alpha$  profiles observed with COS, taken from Henry et al. (2015), Yang et al. (2017a), and Izotov et al. (2016b). The middle row shows the Mg II  $\lambda\lambda 2796, 2803$  doublet, with the velocity scale set relative to the 2796 Å line. The bottom row shows the Si II lines, observed in the same COS spectra as the Ly $\alpha$ . These spectra are ordered with  $f_{esc}^{Ly\alpha}$  increasing from left to right, with measured values given in the upper right hand corner of each Ly $\alpha$  panel. These five galaxies represent the half of the sample with the lowest  $f_{esc}^{Ly\alpha}$ . Dashed vertical lines mark zero velocity for the emission or absorption features. Only some spectra show detectable Si II absorption, and some also show evidence of fluorescent Si II\*  $\lambda\lambda 1194, 1197$  emission (dotted lines). Milky Way contamination from C IV and Co II is noted by grey dot-dashed lines in two of the Si II spectra.

Finally, we combine these observations with COS spectroscopy covering Ly $\alpha$  and FUV absorption lines. We described the data in detail in Henry et al. (2015). In brief, we estimate that the spectral resolution is 20–40 km s $^{-1}$  for compact continuum emission, degraded only somewhat from the optimal point source spectral resolution. Measurements of the Milky Way ISM absorption lines and CIII 1175.5 Å photospheric absorption in the Green Peas implies a redshift precision around 30 km s $^{-1}$ . We rebin the spectra in bins of 20 pixels for continuum and absorption lines (around 45 km s $^{-1}$ ) and 10 pixels for Ly $\alpha$ . Noise in the binned spectra is estimated by summing the photon counts in each bin and calculating the Poisson noise according to Gehrels (1986). The Green Peas 1440+4619 and 1442-0209, which were not originally in the Henry et al. (2015) sample, have been treated in the same manner. We do not correct the COS spectra for aperture losses, which, for Ly $\alpha$ , are mostly unknown, but significant when measured (Henry et al. 2015). As a result, the Ly $\alpha$  measurements give a sense of the flux that escapes from the central few kpc of these compact galaxies.

### 3. ANALYSIS

The Mg II, Ly $\alpha$ , and Si II spectra are shown in Figures 2 and 3. The most striking observation in these figures is the strong Mg II emission and weak (or absent) absorption, similar to the Mg II emitters reported by Erb et al. (2012) and Finley et al. (2017). This finding strongly

suggests that Mg II originates as an emission line, which is not erased by absorption in these galaxies. However, we still see effects of scattering on lines: in each galaxy, the Mg II lines are systematically redshifted. Moreover, the FWHM of the lines range from 100 to 300 km s $^{-1}$ , in some cases, broader than we observe in the optical nebular lines. In contrast, however, we see no evidence that Mg II is extended beyond the continuum (e.g. Rubin et al. 2011; Martin et al. 2013). Remarkably, the Mg II spectra bear no resemblance to the Si II lines shown in the bottom rows of Figures 2 and 3. We will return to this puzzling observation in §4.

#### 3.1. Measurements

To further understand the unusual Mg II emission, we measure fluxes, equivalent widths, peak velocities, and FWHM from these lines. Each spectrum is normalized around the Mg II lines using a linear fit to continuum regions spanning several thousand km s $^{-1}$  around the systemic velocity. We find that the statistical uncertainty on the continuum normalization is a few percent or better, although visual inspection of the data suggests an approximately 5% systematic uncertainty. Next, we divide the spectrum into two regions corresponding to each line, using the midpoint between the two lines,  $\lambda_{rest} = 2799.1$  Å. Bluer wavelengths are assigned to the 2796 Å line while redder wavelengths are assigned to the 2803 Å line. Then, we calculate the equivalent width weighted velocity of each line,  $v_{peak}$ , as a nonparametric means of cen-

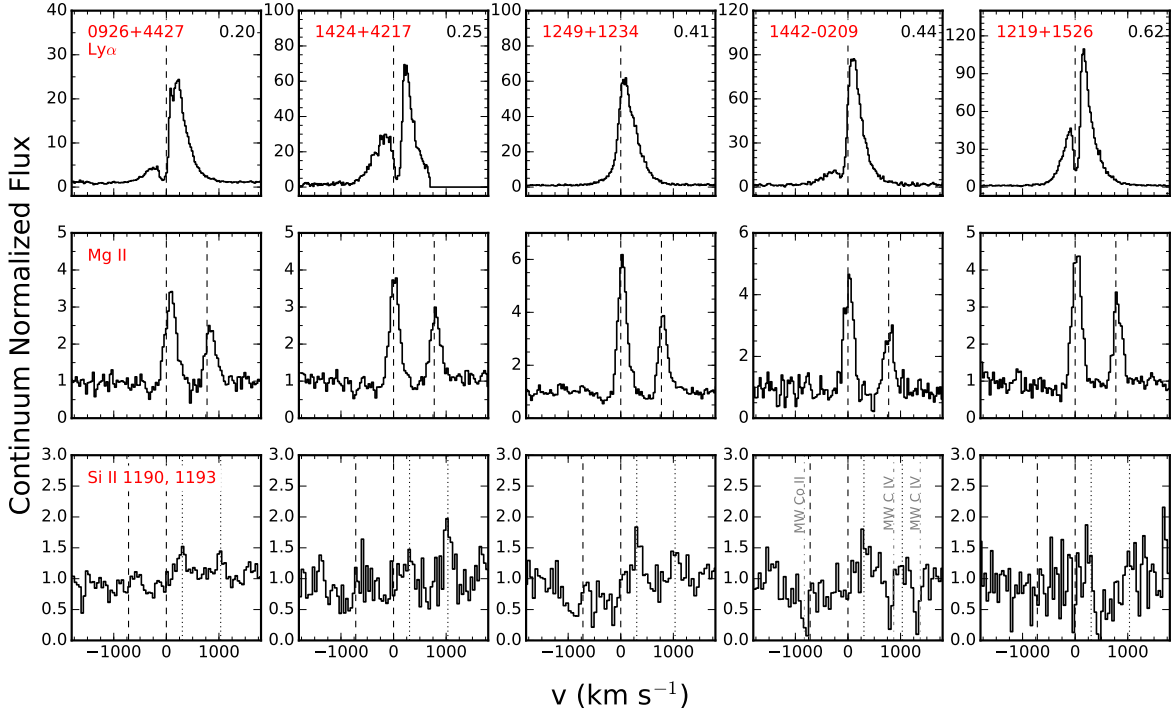


**Figure 3.** Continued from Figure 2. These five galaxies represent the half of the sample with the highest  $f_{esc}^{Ly\alpha}$ .

troiding the emission (see Henry et al. 2015). Since some lines show minimal absorption blueward of the 2796 Å line, we measure a blueshifted velocity where the absorption meets the continuum. For the 2796 Å line, the fluxes and equivalent widths are integrated to this maximal velocity. In the case of 1440+4619, the emission is mostly erased by this absorption. Finally, errors are calculated through a Monte Carlo simulation where we perturb the spectrum according to its errors, repeat the measurements, and calculate the RMS.

The Mg II measurements are likely impacted by stellar Mg II absorption. Martin & Bouché (2009) highlight how this absorption varies with the characteristic age of the stellar population, showing that weaker absorption corresponds to younger stellar populations. In order to quantify this absorption for the present sample, we measured the absorption equivalent width in the Binary Population and Spectral Synthesis (BPASS v2.0; Eldridge & Stanway 2009) models that we use for photoionization modeling in §3.2 (see below). At the resolution of these models, the Mg II lines are blended. Nevertheless, we find a minimum  $W_{stellar} = 0.2$  at ages of a few Myr (for both bursts and continuous star-forming models). An upper limit on  $W_{stellar}$  can be inferred by considering the maximum plausible ages that can still produce  $W_{H\alpha} \gtrsim 300$  Å, typical for Green Peas. This requirement implies that the ages can be at most a few hundred Myrs for continuous star-forming models, which corresponds to  $W_{stellar} < 1.0$  in the BPASS models considered here. Therefore, we adopt  $W_{stellar} = 0.6$ ; since the Mg II lines are unresolved in the stellar models, we apply a 0.3 Å correction to the equivalent width of each Mg II line, and scale the measured fluxes accordingly. The Mg II measurements are presented in Table 3.

For the COS spectra, we compile several measurements

from Henry et al. (2015), repeating that analysis for 1440+4619 and 1442-0209. First, we include the Ly $\alpha$  escape fractions,  $f_{esc}^{Ly\alpha} = F(Ly\alpha) / (8.7 \times F(H\alpha)_{corr})$ , where  $F(H\alpha)_{corr}$  is corrected for dust (according to Calzetti et al. 2000). For this calculation, we use an intrinsic Ly $\alpha$ /H $\alpha$  ratio of 8.7, since these Green Pea galaxies have elevated electron densities ( $n_e = 100 - 700$  cm $^{-3}$ ), which increases Ly $\alpha$ /H $\alpha$  above the Case-B low density limit of 8.1 (Dopita & Sutherland 2003; Henry et al. 2015). The Ly $\alpha$ , Mg II, and Si II spectra in Figures 2 and 3 are shown in order of increasing  $f_{esc}^{Ly\alpha}$ . Second, in addition to Ly $\alpha$  escape fractions, we include kinematic measures for the Ly $\alpha$  lines. We measure the peak velocities,  $v_{blue}^{peak}$  and  $v_{red}^{peak}$ , since peak separation is sensitive to the H I column density (Verhamme et al. 2015), and has been shown to correlate with  $f_{esc}^{Ly\alpha}$  (Henry et al. 2015). Finally, velocities and equivalent widths of FUV absorption can also be compared to Mg II. For 1440+4619 and 1442-0209, we either do not convincingly detect the low-ionization (LIS) metal absorption lines (Si II and C II) that trace H I, or we find that the spectra are contaminated by foreground Milky Way absorption. Therefore, we either set upper limits on the equivalent widths at  $W_{LIS} \gtrsim -0.5$  Å, or exclude the lines. For the remainder, we take the measurements from Henry et al. (2015), and do not reproduce that tabular data here. Since these lines are often weak in Green Peas and similar galaxies (Erb et al. 2010; Henry et al. 2015; Chisholm et al. 2017), we mostly focus on Ly $\alpha$  in this paper, but we do consider whether Mg II varies with  $W_{LIS}$  in §4. To conclude, the Mg II and Ly $\alpha$  measurements are reported in Tables 2 and 3.

### 3.2. Calculating Mg II Escape Fractions with Photoionization Models

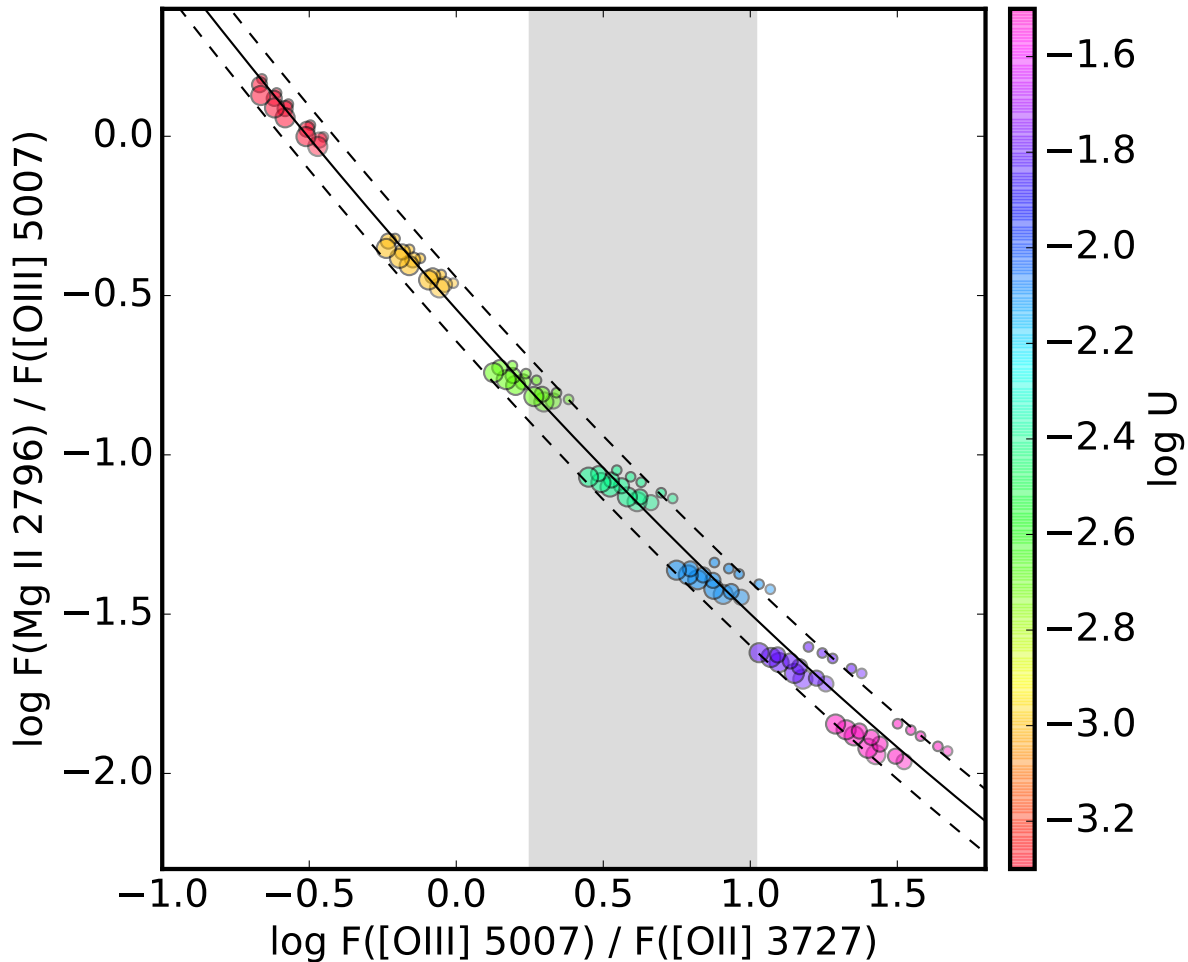


**Figure 4.** Cloudy photoionization models show that Mg II/[O III] forms a tight sequence with [O III]/[O II]. For simplicity, and since all BPASS and Starburst99 models fall along the same sequence, we show only a subset of the BPASS (version 2.0) models, using the continuous star-formation histories, a  $100 M_{\odot}$  upper mass cutoff, and  $n_e = 10^{2.4} \text{ cm}^{-3}$ . The grey shaded region shows the range of [O III]/[O II] values covered by our sample. The different colored points highlight the variations in ionization parameter,  $U$ , and the point sizes are proportional to the gas-phase metallicity ( $Z/Z_{\odot} = 0.1, 0.25, 0.4$ ). Each grid point ( $\log U$  and gas-phase metallicity) is plotted for five stellar metallicities ( $Z = 0.001, 0.002, 0.004, 0.006, \text{ and } 0.008$ ). In these models, the harder ionizing spectrum at lower stellar metallicities moves the line ratios downwards along the sequence. The solid line indicates the polynomial fits to the BPASS models (Equations 1 and 2), while the dashed lines mark  $\pm 0.1$  dex

In order to understand how the observed Mg II varies due to scattering and absorption in the ISM and CGM, we must first account for the intrinsic variations in the Mg II produced in H II regions. Therefore, we aim to predict the intrinsic Mg II fluxes, using photoionization models constrained by the physical properties determined from the SDSS spectra (i.e., oxygen abundance and electron density,  $n_e$ ). Fortunately, for the Green Peas in our sample, significant detections of the temperature-sensitive [O III]  $\lambda 4363$  auroral line allow accurate determinations of the oxygen abundance using the “direct” method<sup>8</sup>. We follow the procedure described in

<sup>8</sup> While there has been a long-standing debate over the accuracy of the “direct” method, recent studies have shown remarkable agreement between stellar and “direct” method nebular abundances in typical nearby galaxies (Davies et al. 2017; Zahid et al. 2017). Therefore, we judge the gas-phase metallicity calibration as accurate to around 0.2 dex.

Berg et al. (2015)<sup>9</sup> to determine electron densities and direct method abundances. For this calculation, we correct the emission lines for internal dust attenuation using the reddening law of Calzetti et al. (2000), and also use the theoretical Garnett (1992) relationship to estimate the [O II] electron temperature from the measured [O III] temperature. The electron densities were measured from the [S II]  $\lambda\lambda 6716, 6731$  doublet, and ranged from  $100\text{--}700 \text{ cm}^{-3}$ . The metallicities are between  $12 + \log(\text{O}/\text{H}) = 7.9$  to  $8.2$  ( $Z_{\text{gas}} = 0.16 - 0.32Z_{\odot}$ , where  $Z_{\odot}$  corresponds to  $12 + \log(\text{O}/\text{H}) = 8.69$ ; Grevesse et al. 2010), and are listed in Table 2.

For photoionization modeling, we use Cloudy version 17 (Ferland et al. 2017), considering a range of ionizing spectra with sub-solar metallicities. First, we in-

<sup>9</sup> Specifically, we use the IDL-based IMPRO routines (<https://github.com/moustakas/impro>), along with the atomic data in Berg et al. (2015).

clude fourteen models from Starburst99 (Leitherer et al. 1999, 2014). In brief, these are: the Padova models, with and without AGB stars, at  $Z_{stars} = 0.0004, 0.004, 0.008$  ( $Z = 0.029, 0.29,$  and  $0.57 Z_{\odot}$ , where  $Z_{\odot} = 0.014$ ); the Geneva models with standard and high mass loss rates at  $Z_{stars} = 0.001, 0.004, 0.008$ ; and the Geneva models with and without rotation at  $Z_{stars} = 0.002$  ( $Z = 0.14 Z_{\odot}$ ). In all Starburst99 models, we use the Kroupa (2001) stellar initial mass function (IMF). Second, we consider the Binary Population and Spectral Synthesis models (BPASS v2.0 and v2.1; Eldridge & Stanway 2009; Eldridge et al. 2017), which include the effects of binary evolution and produce harder ionizing spectra than Starburst99. For these models, we include metallicities of  $Z_{stars} = 0.001, 0.002, 0.004, 0.008$  ( $Z = 0.07, 0.14, 0.29$  and  $0.57 Z_{\odot}$ ) and use the fiducial IMF, which has a slope of  $-1.30$  between  $0.1$  and  $0.5 M_{\odot}$  and  $-2.35$  above  $0.5 M_{\odot}$ . For BPASS v2.1, we also include the  $Z_{stars} = 10^{-4}$  and  $10^{-5}$  models. For all BPASS models, we consider the IMFs both with  $100$  and  $300 M_{\odot}$ . Finally, we select both constant star-forming models and bursts aged  $1, 3,$  and  $10$  Myrs for both BPASS and Starburst99, except for BPASS v2.1, where only the bursts are available.

Following Steidel et al. (2016), the photoionization models were run using a plane-parallel geometry. The ionization parameter,  $U$ , was varied between  $-3.3 < \log U < -1.5$  in  $0.3$  dex increments. Models were calculated for three gas-phase metallicities, allowing for systematic uncertainties by covering a slightly broader range than our measurements:  $Z_{gas} = 0.1, 0.25,$  and  $0.4 Z_{\odot}$ . Likewise, we calculated models over the range of densities measured for our sample:  $n_e = 10^{2.0}, 10^{2.4},$  and  $10^{2.8} \text{ cm}^{-3}$ . Finally, we chose the Orion dust grains, and a solar relative abundance pattern (Grevesse et al. 2010). Here, we do not require the stellar and gas-phase metallicities to match, as non-solar  $\alpha/\text{Fe}$  abundances can give the appearance of decoupled stellar and nebular metallicities (Steidel et al. 2016).

We explored a number of line diagnostic diagrams in order to predict Mg II from the optical spectrum of the Green Peas. This exercise showed that Mg II/[O III]  $\lambda 5007$  forms a tight sequence with the ratio [O III]  $\lambda 5007$ /[O II]  $\lambda 3727$ , as illustrated in Figure 4. Here, we show Mg II  $\lambda 2796$  / [O III]  $\lambda 5007$ . The same plot with Mg II  $\lambda 2803$  / [O III]  $\lambda 5007$  appears similar, with only a factor of two difference set by the intrinsic Mg II  $\lambda 2796$  / Mg II  $\lambda 2803$  ratio. We find that this sequence does not depend on the stellar model, as harder ionizing spectra move the line ratios down and to the right *along* the sequence. This effect can be seen in Figure 4, as each set of colored points (a single ionization parameter) is shown in a cluster of 5 “rows”, each corresponding to a BPASS v2.0 model with a different stellar metallicity. Likewise, gas-phase metallicity moves the line ratios roughly orthogonally to the sequence. Hence, metallicity plays a key role in setting the scatter in Figure 4. We have conservatively considered gas-phase metallicities  $0.1$  dex lower and higher than we have measured, as we will use this scatter below to estimate the uncertainty on the predicted intrinsic Mg II flux.

Figure 4 shows only continuous star-forming BPASS models with  $n_e = 10^{2.4}$ . Nevertheless, for the ionizing spectra with sub-solar metallicities that we consider here,

all reasonable Starburst99 and BPASS models fall along the same sequence, regardless of star-formation history or IMF upper limit. Still, we verified that this sequence is robust to several other changes in the models. First, changing  $n_e$  shifted the line ratios by only a negligible amount. Second, we considered the effects of reduced dust depletion, as De Cia et al. (2016) show that dust-to-metal ratios may be lower at lower metallicity. We ran a subset of Cloudy models with no grains, finding that Mg II/[O III] ratios would be higher by around  $0.1$ - $0.2$  dex over the O32 range covered by our sample. However, since this limiting case is extreme, we infer that uncertainties in dust depletion probably lead to line ratios that fall within the  $0.1$  dex scatter in Figure 4. Third, we explored how an active galactic nucleus (AGN) may impact the inference of intrinsic Mg II. We ran Cloudy models, extending to gas-phase metallicity of  $Z_{gas} = 2.0 Z_{\odot}$ , and using Cloudy’s default AGN spectral template:  $T = 1.5 \times 10^5$  K for the “Big Bump” component, an X-ray to UV ratio,  $\alpha_{ox} = -1.4$ , and the low-energy slope of  $\alpha_{uv} = -0.5$ . We find that the O32 range covered by our sample is reached at super solar gas-phase metallicities, with Mg II/[O III] ratios  $0.2$ - $0.3$  dex lower than the sequence in Figure 4. Therefore, this AGN model would predict weaker intrinsic Mg II emission by a factor of  $1.5$ - $2$ , possibly even weaker than the observed Mg II fluxes. We note, however, that the Green Peas show no evidence for the presence of an AGN. Finally, we tested some ionizing spectra with super-solar metallicities, and found a number of model grid-points may fall below the tight sequence in Figure 4. Likewise, the  $10$  Myr aged burst, with BPASS v2.1 spectra does not produce realistic line ratios for the Green Peas (e.g. [O III]/H $\beta$  < 1). Hence, we exclude these models from consideration. We conclude that the sequence in Figure 4 should be robust for our sample.

Figure 4 demonstrates that, with [O III]  $\lambda 5007$ /[O II]  $\lambda 3727$  alone, we can predict the intrinsic Mg II/[O III]  $\lambda 5007$  to within  $0.1$  dex for these Green Peas. This figure also shows the polynomial fit to our full set of BPASS v2.0 model grids, for the IMF with a  $100 M_{\odot}$  upper mass cutoff. These relations are:

$$R_{2796} = 0.079 \times \text{O32}^2 - 1.04 \times \text{O32} - 0.54 \quad (1)$$

and

$$R_{2803} = 0.098 \times \text{O32}^2 - 1.02 \times \text{O32} - 0.84, \quad (2)$$

where

$$\begin{aligned} R_{2796} &= \log (\text{Mg II } \lambda 2796 / [\text{OIII}] \lambda 5007), \\ R_{2803} &= \log (\text{Mg II } \lambda 2803 / [\text{OIII}] \lambda 5007), \end{aligned} \quad (3)$$

and

$$\text{O32} = \log ([\text{OIII}] \lambda 5007 / [\text{OII}] \lambda 3727).$$

We reiterate that these relations are valid over the gas-phase metallicities that we consider here:  $12 + \log(\text{O}/\text{H}) = 7.8 - 8.3$  ( $Z = 0.1 - 0.4 Z_{\odot}$ ). Higher gas-phase metallicities tend to move points down and to the left in Figure 4, increasing the scatter to a value more like  $0.2$  dex. In this case, deriving a unique best-fitting Cloudy model for each galaxy may be a better strategy than using the relations given here.

Finally, given the intrinsic Mg II/[O III]  $\lambda 5007$  ratios,

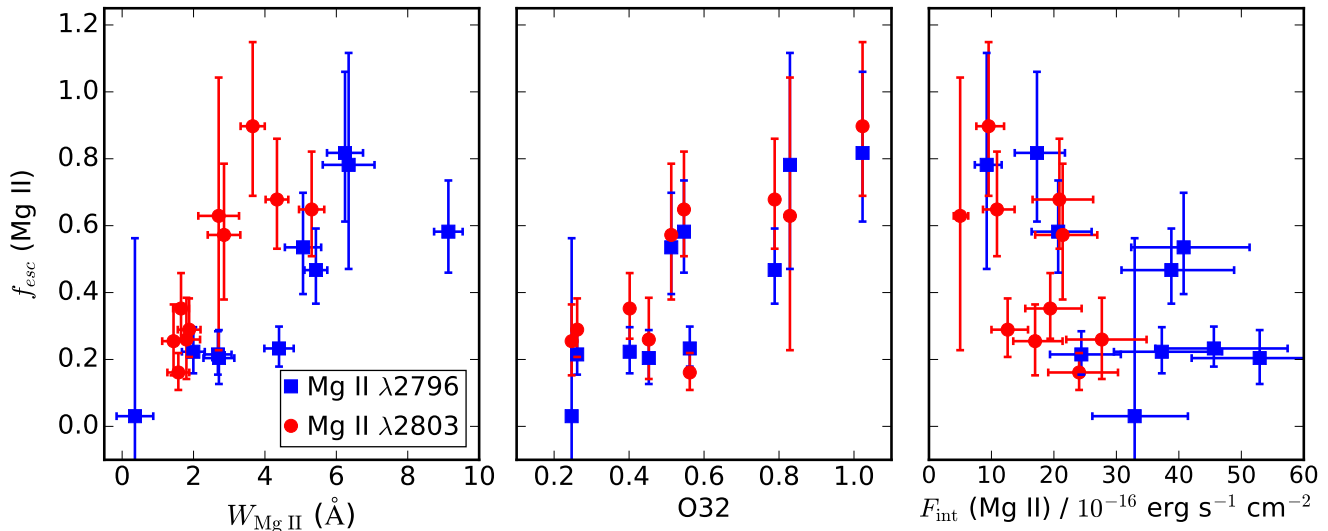


**Figure 5.** *Left*– The escape fraction of the Mg II lines correlates with their equivalent width, indicating that stronger emission results from greater escape rather than intrinsically strong emission. *Center*– Higher Mg II escape fraction is also associated with higher O32 ( $\equiv [\text{O III}] \lambda 5007 / [\text{O II}] \lambda 3727$ ) ratios, leading to weaker Mg II/[O III] ratios (following Figure 4 and Equations 1 and 2). *Right*– These weaker Mg II/[O III] ratios translate to fainter intrinsic Mg II flux in the sources with the highest Mg II escape fractions. In all panels, the uncertainties on the Mg II escape fraction include a 0.1 dex uncertainty on the predicted intrinsic Mg II flux, added in quadrature to the measurement error.

we can calculate the fraction of Mg II photons that escape the galaxies. We use the [O III] and [O II] lines (corrected for dust using Calzetti et al. 2000) to predict the intrinsic Mg II for each line of the doublet, in each galaxy. Then, we calculate the escape fractions by comparing observed and intrinsic line fluxes:

$$f_{esc}^{2796} = F^{obs}(\text{Mg II } 2796) / F^{int}(\text{Mg II } 2796) \quad \text{and} \quad (4)$$

$$f_{esc}^{2803} = F^{obs}(\text{Mg II } 2803) / F^{int}(\text{Mg II } 2803).$$

In this calculation, the observed Mg II fluxes are corrected for slit-losses as described in §2. We also correct for Milky Way foreground extinction, using the Fitzpatrick (1999) attenuation curve and the extinction values from (Schlafly & Finkbeiner 2011;  $E(B-V)_{MW}$  listed in Table 1). Additionally, we note that the uncertainty on Mg II escape fraction includes the statistical error on the line fluxes and the 0.1 dex uncertainty on the intrinsic Mg II prediction. We do not, however, include an error to account for systematic uncertainties in the internal extinction law, as this error is ill-defined. Although we chose Calzetti et al. (2000), we note that other attenuation curves (e.g. SMC, LMC; Gordon et al. 2003, Milky Way; Cardelli et al. 1989; Fitzpatrick 1999) predict smaller absolute dust corrections, leading to lower intrinsic [O III] fluxes and up to 25% higher Mg II escape fractions. The Mg II escape fractions are given in Table 3.

Overall, our calculation of Mg II escape fractions is analogous to the calculation of Ly $\alpha$  escape fractions in its treatment of dust. The Cloudy models presented in Figure 4, and the relations in Equation 1 and 2 use intrinsic line fluxes, rather than dust attenuated. Likewise, the observed Ly $\alpha$  and Mg II line fluxes are not corrected for internal dust extinction, since a robust correction is difficult to discern when photons are resonantly scattered. Therefore, like Ly $\alpha$ , an escape fraction less than unity

implies that photons are absorbed by dust, or scattered outside the aperture.

We judge these estimates to be accurate in a relative sense, but acknowledge that photoionization modeling of the intrinsic line fluxes is subject to systematic uncertainties. Different assumptions about relative abundance ratios, dust depletion patterns, and shocks may predict systematically different intrinsic Mg II emission. Hence, we urge caution, and focus on qualitative trends going forward.

#### 4. CHARACTERIZING MG II ESCAPE

The Green Peas in this sample show a range of Mg II equivalent widths (0 to 9 Å) and escape fractions (0 to 0.9). Figure 5 explores the cause of these variations. First, the left-hand panel shows that Mg II equivalent widths correlate with escape fractions. This trend implies that higher Mg II equivalent width emission is not necessarily an indication that Mg II is intrinsically stronger; rather, the ISM is more transparent to Mg II when the equivalent width is higher. In fact, the center panel of Figure 5 shows that the sources with the strongest Mg II emission have higher O32 values. In our Cloudy models (and according to Equations 1 and 2), the higher O32 values are an indication of weaker Mg II/[O III] ratios. These lower Mg II/[O III] ratios translate directly to fainter intrinsic Mg II emission for the sources that have the highest equivalent widths and escape fractions (Figure 5, right). In summary, the sources with the strongest *observed* Mg II emission are actually those with the weakest *intrinsic* emission.

We next look for signs of resonant line radiation transport on the Mg II lines. Figure 6 presents the Mg II escape fractions for the 10 Green Peas in this sample, comparing the two lines of the doublet. The ratio of oscillator strengths describing the ISM absorption on these lines is  $f_{2796} / f_{2803} = 0.61 / 0.30$ , or about a factor of two. Hence, the optical depths are related:  $\tau_{2796} = 2 \times \tau_{2803}$ . How-

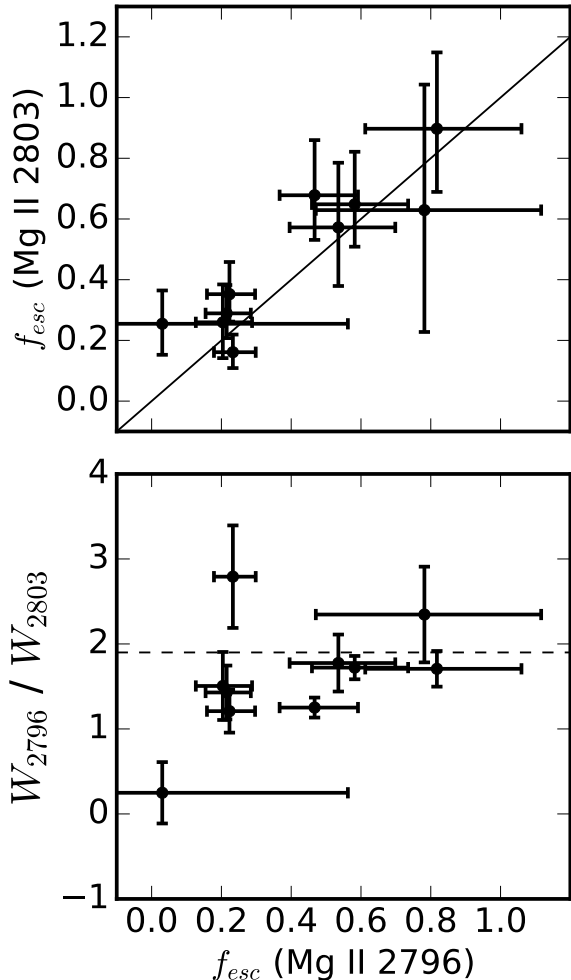


**Figure 6.** *Top:* The Mg II  $\lambda 2796$  and  $\lambda 2803$  escape fractions are consistent, within the errors, for most of the galaxies in the present sample. *Bottom:* The equivalent widths of the lines are close to the intrinsic ratio of about 1.9 (dashed line). The Mg II  $\lambda 2796$  line is intrinsically stronger in H II regions, but its ISM optical depth is two times higher than the 2803 Å line. These observations indicate that, given the competing effects of ISM absorption and intrinsic emission, absorption is not very significant in setting the doublet ratio in these galaxies.

ever, since these lines are resonant, the optical depths do not necessarily translate into differing escape fractions. Rather, the top panel of Figure 6 shows the escape fractions of the lines are mostly consistent within the errors, except for the galaxy with the **highest dust extinction** and lowest escape fraction in the  $\lambda 2796$  line: 1440+4619. In this case, although we detect Mg II emission, we also detect absorption on the  $\lambda 2796$  line, so the net equivalent width is near zero (before the stellar absorption correction). Similarly, the bottom panel of Figure 6 shows that the equivalent width ratios,  $W_{2796}/W_{2803}$ , are near the intrinsic ratio of about 1.9, inferred from our Cloudy models. Overall, it appears that the effects of resonant scattering are not significant enough to alter the intrinsic line ratio, or cause the  $\lambda 2796$  line to have a lower escape fraction.

While the Mg II equivalent width and escape fraction

ratios indicate that photon scattering is insufficient to remove  $\lambda 2796$  photons more than  $\lambda 2803$  photons, kinematic measures, in contrast, show evidence of radiation transport. As noted in §3, and shown in Figures 2 and 3, the Mg II lines are systematically redshifted by an average of  $70 \text{ km s}^{-1}$ . Additionally, in a few cases the Mg II lines are broader than the optical nebular lines. While the SDSS spectral lines are only marginally resolved, we have obtained Keck/ESI spectra for the 8/10 Green Peas in the present sample, achieving  $75 \text{ km s}^{-1}$  spectral resolution (Henry et al., in prep). After correcting for spectral resolution, we find that the Green Pea 1244+0216 has FWHM of  $327 \pm 44$  and  $195 \pm 119$  for the  $\lambda 2796$  and  $\lambda 2803$  lines, respectively, whereas its H $\beta$  line has a FWHM of only  $94 \text{ km s}^{-1}$ . Likewise, 1249+1234 has FWHM around  $122 \pm 35 \text{ km s}^{-1}$  in both Mg II lines, compared to  $66 \text{ km s}^{-1}$  in H $\beta$ . Lastly, the  $\lambda 2796$  line of 0926+4427 has FWHM of  $208 \pm 46$ , whereas H $\beta$  is substantially narrower at  $106 \text{ km s}^{-1}$ . For 1440+4619 and 1442-0209, we do not have a high resolution spectrum for comparison, but we do note that 1440+4619 has Mg II lines which are among the broadest in our sample, similar to 1244+0216.

The broad widths and redshifted emission are analogous to the case of Ly $\alpha$ . Therefore, we may expect the lines to be more redshifted and broadened when the column density of Mg II is higher, and the escape fractions are lower. The top panels of Figure 7 test this hypothesis, showing a tentative relation in the expected direction: higher Mg II escape fraction may be associated with lower Mg II peak velocities and smaller FWHM. The bottom panels of Figure 7 show the same kinematic measures against the Ly $\alpha$  escape fraction, with a similar tentative correlation. The Pearson correlation coefficient ( $\rho$ ), and probability of the null hypothesis (P) are shown in each panel, indicating a 2-8% likelihood of a spurious correlation. Additional observations could clarify this relation. Not only would a broader dynamic range be useful, it is also clear that high-resolution and high signal-to-noise will be needed to measure Mg II peak velocity shifts of order  $100 \text{ km s}^{-1}$ .

A more detailed look at the Mg II line profiles is shown in Figure 8. Here we compare the Mg II and H $\beta$  lines of two Green Peas, bracketing the range of escape fractions probed by our sample. This comparison shows clearly that 1244+0216, which is among the Green Peas with the lowest Ly $\alpha$  escape fractions, widest Ly $\alpha$  peak separations, and lowest Mg II escape fractions, has much broader Mg II than H $\beta$ . On the other hand, 1219+1526, which has properties similar to Lyman Continuum leakers (Verhamme et al. 2017), is only marginally broadened on the red side of the Mg II lines. The spectral resolution is comparable between the two observations ( $90 \text{ km s}^{-1}$  for the Mg II spectrum and  $75 \text{ km s}^{-1}$  for the H $\beta$ ), so the broader Mg II lines cannot be due to instrumental effects. We also notice in Figure 8 that 1244+0216 has double peaked Mg II emission on both lines of the doublet. Here, we are detecting the same effect that shapes the Ly $\alpha$  profiles of the Green Peas: due to the relatively high optical depth at line center, photons scatter away from the systemic velocity and into the wings of the lines. Indeed, the somewhat wider peak separation for the  $\lambda 2796$  line ( $200 \pm 20 \text{ km s}^{-1}$  vs  $170 \pm 40 \text{ km s}^{-1}$ ) is consistent with its

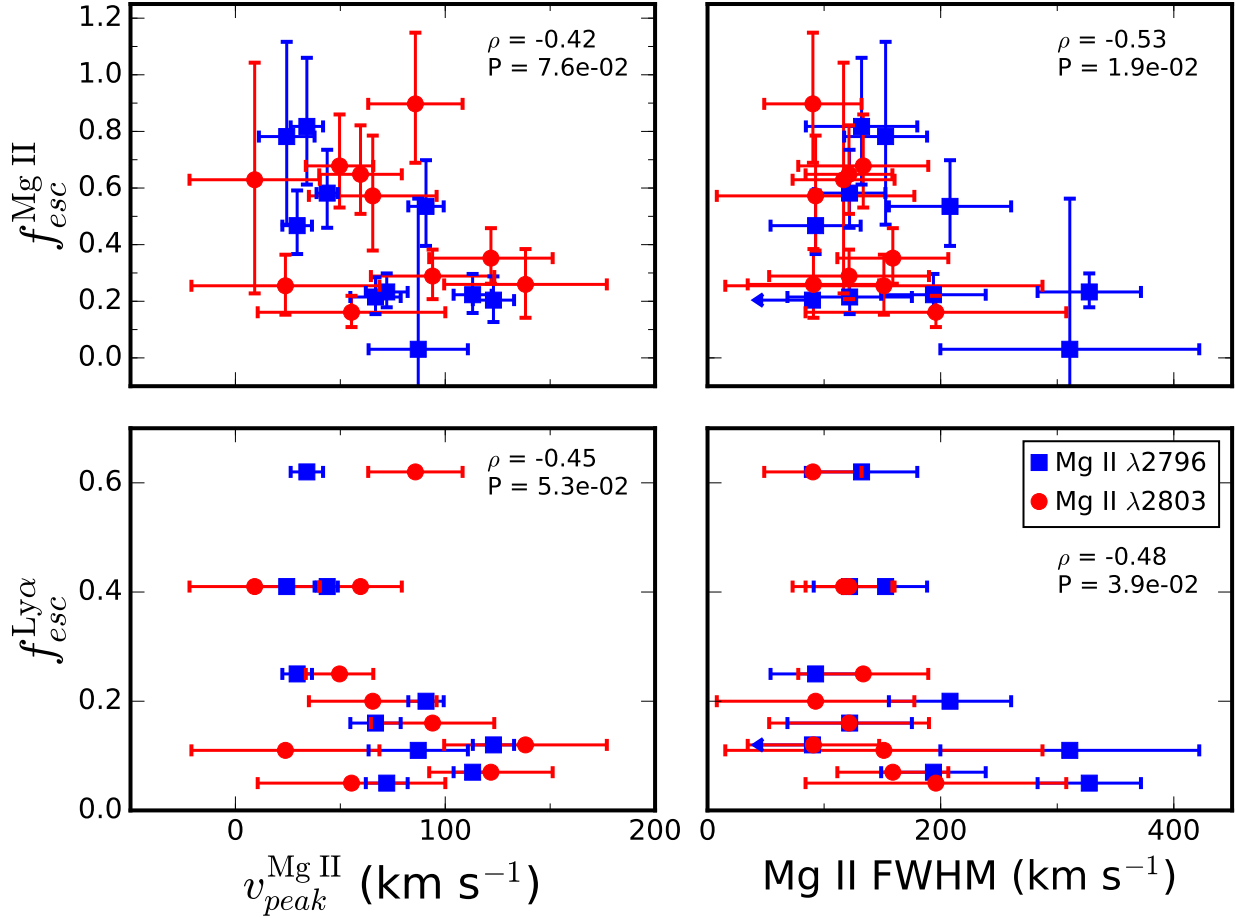


**Figure 7.** Mg II and Ly $\alpha$  escape fractions show a tentative relation with Mg II FWHM and peak velocity shift. These correlations are expected if the escape fractions are determined by low column density of neutral and low-ionization state gas. When the column densities are low, the redshifting and broadening of the Mg II lines should be lessened. The Pearson correlation coefficient,  $\rho$ , and the probability of the a spurious correlation,  $P$ , are given in each panel. The Mg II FWHM are corrected for instrumental resolution.

higher oscillator strength and optical depth to ISM absorption, relative to the  $\lambda 2803$  line. Overall, we conclude that the changes in the peak velocities and FWHM are consistent with a scenario of varying column densities of neutral and low ionization state gas.

Next, we explore the role of dust extinction in establishing the Mg II emission. Figure 9 shows trends where lower dust extinction is associated with higher Mg II equivalent width and escape fraction. Again, the Pearson correlation coefficients are given in each panel, alongside the probability of a spurious correlation. Although any correlation is only tentative, the trends follow our expectations. For comparison, we show the starburst dust extinction law from Calzetti et al. (2000), along with the Small Magellanic Cloud (SMC), and Large Magellanic Cloud (LMC) from Gordon et al. (2003). While non-resonant lines should follow the appropriate extinction curves, resonant lines are more susceptible to dust attenuation because multiple scatterings increase the likelihood of absorption. Hence, it is not surprising that many of the Mg II and Ly $\alpha$  escape fractions fall below the relevant curves in Figure 9. While about half the sample lies near the locus where dust extinction alone could explain the Mg II escape fractions, the other half

appears to have too little Mg II emission for the amount of extinction. However, we again caution that the Mg II escape fractions are uncertain in an absolute sense, due to systematics associated with the photoionization modeling and intrinsic Mg II flux derivation. Likewise, as we noted in §3.2, using an SMC, LMC, or Milky Way dust attenuation curve when estimating intrinsic Mg II flux (from dust-corrected [O III]) could increase the Mg II escape fraction by up to 25% in the sources with the most dust. Nevertheless, since we do see effects of resonant-line radiation transport on the line profiles, we conclude that the less-than-unity Mg II escape fractions should probably not be explained by dust extinction without resonant scattering.

Since Ly $\alpha$  and Mg II are both shaped by scattering in low-ionization state gas, we might expect their escape fractions to be related. Indeed, Figure 10 verifies this hypothesis. The left panel shows that  $W_{Mg II}$  correlates with  $W_{Ly\alpha}$ , while the right panel shows a tight relation between  $f_{esc}^{Ly\alpha}$  and the Mg II escape fractions. The Pearson correlation coefficient, and probability of the null hypothesis are listed in each panel. The relation between the escape fractions—where we have included both Mg II lines in the correlation—is especially robust, with the

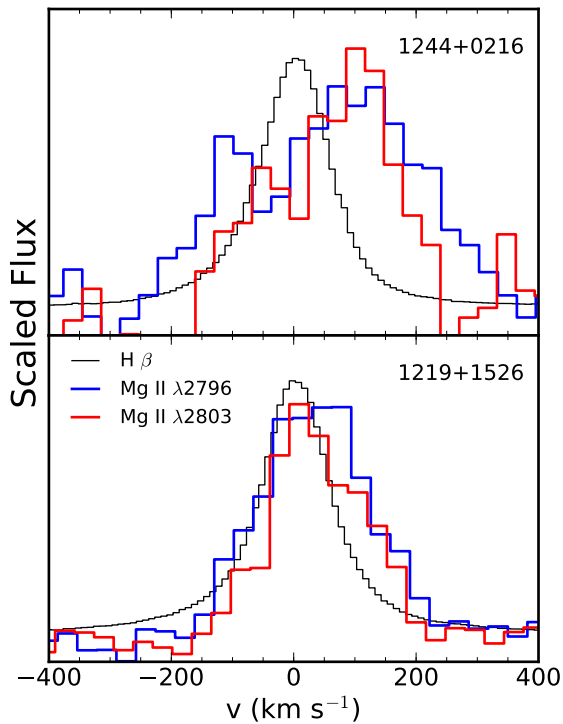


**Figure 8.** Mg II profiles are compared to H $\beta$  for two Green Peas. The cases highlighted here bracket the range of Mg II and Ly $\alpha$  escape fractions probed by our sample. Consistent with having higher column densities of low-ionization state gas, the Green Pea 1244+0216 has double peaked profiles, much broader than H $\beta$ . On the other hand, 1219+1526, which has properties consistent with LyC Leakers (Verhamme et al. 2017), shows Mg II profiles that are mostly symmetric and only marginally broader than H $\beta$  on the red side. The line fluxes are scaled arbitrarily to compare the profiles.

probability of a spurious correlation around  $10^{-7}$ . A linear fit to these data indicates that:

$$f_{esc}^{Mg II} = 0.13 + 1.21 f_{esc}^{Ly\alpha}, \quad (5)$$

where both Mg II lines are included in the fit. These correlations are notable: they confirm that the Ly $\alpha$  and Mg II escape are regulated by resonant scattering in the same gas. Since high Ly $\alpha$  escape fractions can be a sign of low column densities of H I gas (Verhamme et al. 2015), we infer that high Mg II escape must also be a sign of correspondingly low column densities of Mg II. Remarkably, a link between Ly $\alpha$  and Mg II (and the column density of low ionization state gas) opens up the potential for a new diagnostic in the reionization epoch, where Ly $\alpha$  and Lyman Continuum are difficult to observe. We will return to this point in §5.

While a relationship between Mg II and Ly $\alpha$  escape fractions is sensible, the observation that these quantities are of the same order is counterintuitive. The Ly $\alpha$  and Mg II transitions have optical depths to resonant scattering which differ by orders of magnitude. Hence, one might expect a substantially lower  $f_{esc}^{Ly\alpha}$  for a given Mg II escape fraction. Considering dust attenuation highlights this puzzling observation. Figure 10 shows the predicted relationship between the Ly $\alpha$  and Mg II, if the lines were non-resonant, for three extinction curves. All three run through our observations. Yet, because Ly $\alpha$

scatters much more than Mg II, we expect it to be much more impacted by dust. This effect would place the measurements to the left of the extinction curves. Although Figure 9 suggests that the Mg II and Ly $\alpha$  emission see more dust than a non-resonant photon would (for at least some of the sample), contrary to our expectation, Figure 10 suggests that this effect is *not* more pronounced for Ly $\alpha$  than it is for Mg II. The reason for this observation is unclear. While similar escape fractions could arise from a scenario where the Ly $\alpha$  and Mg II photons escape through pathways with negligible column densities of low-ionization state gas (and dust), we previously showed that Green Peas have uniformly high covering and modest column densities ( $N > 10^{16} \text{ cm}^{-2}$ ) in H I (Henry et al. 2015). Similarly, Scarlata et al. (2009) showed that, for  $z \sim 0.3$  Ly $\alpha$  emitters, there was no need to invoke a scenario where the Ly $\alpha$  photons escape through dust-free “holes” in the ISM. Therefore, we conclude that more detailed radiation transport modeling would be helpful.

Even with Mg II showing similarities to Ly $\alpha$ , it is surprising how little it resembles the Si II  $\lambda\lambda 1190, 1193$  profiles that we show in Figures 2 and 3. With similar ionization potentials and abundances (assuming a solar relative abundance pattern; Grevesse et al. 2010) the column densities of Mg II and Si II should be comparable. However, there are two notable differences between these spectral features. First, Si II  $\lambda\lambda 1190, 1193$  is not produced appreciably in H II regions. The Cloudy models presented in §3.2 show that Si II  $\lambda\lambda 1190, 1193$  is 1-3 dex fainter than Mg II  $\lambda\lambda 2796, 2803$  in almost all cases. Only the 10 Myr aged instantaneous bursts with  $\log U > -2.0$  can have Si II lines comparable in strength to Mg II; however, this combination of parameters is probably unphysical, as such high ionization parameters are implausible for models that lack O stars. So we can conclude that the nebular origin for Mg II is not matched by Si II. The second difference between Mg II and Si II is resonant trapping of the line and continuum photons. For the Si II feature, fluorescent fine structure Si II\* lines at  $\lambda 1194$  and  $\lambda 1197 \text{ \AA}$  are coupled with the Si II  $\lambda\lambda 1190, 1193$  lines. Photons absorbed in the resonant line can escape through a non-resonant channel, rather than filling in the absorption in the resonant line. Since Mg II lacks this non-resonant channel, the absorption is entirely filled by re-emission (as with Ly $\alpha$ ). Given these two major differences, we can understand that the line profiles will appear very different in some cases. Still, a single, self-consistent model (e.g. Scarlata & Panagia 2015) should be able to reproduce the Mg II, Si II, and Si II\* when these considerations are taken into account.

Despite the lack of any qualitative similarities between the Si II and Mg II line profiles in Figures 2 and 3, a quantitative relationship may be expected when we take the Mg II escape fractions into account. Figure 11 takes the analogy between Ly $\alpha$  and Mg II one step further. Equivalent widths in the low-ionization interstellar (LIS) metal absorption lines have been shown to correlate with Ly $\alpha$  equivalent width or escape fraction (Shapley et al. 2003; Chisholm et al. 2017). For high redshift populations, the interpretation is that the equivalent width of the LIS lines measures the fraction of the background source covered by absorbing ISM (Shapley et al. 2003;

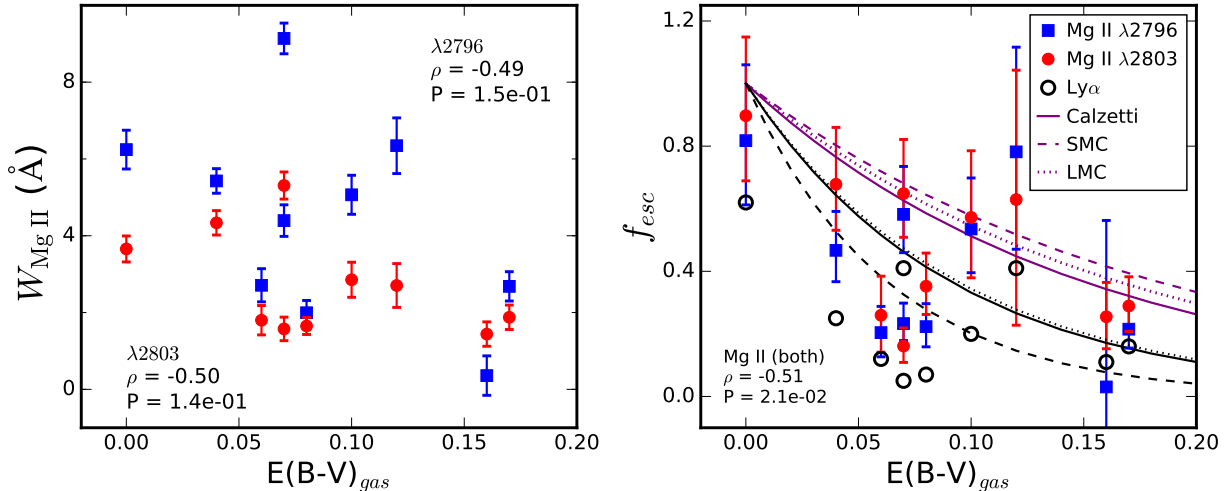


**Figure 9.** The Mg II equivalent width and escape fraction are somewhat higher when dust extinction is lower. The black points show that this trend mirrors the relation seen in Ly $\alpha$ . The Pearson correlation coefficient,  $\rho$ , and the probability of a spurious correlation are given in each panel, indicating only marginally significant trends. Extinction curves from Calzetti et al. (2000), and the SMC and LMC (Gordon et al. 2003) are shown in purple for Mg II and black for Ly $\alpha$ . Despite the tentative correlation, the measured points show a general trend expected if dust plays a role in setting Mg II and Ly $\alpha$  escape. The fact that the many measurements fall below the extinction curves is an expectation for resonant lines, which are more susceptible to dust extinction than non-resonant lines.

Jones et al. 2012, 2013). Hence, weaker LIS lines may indicate lower covering fractions, which facilitate higher Ly $\alpha$  escape fractions and equivalent widths. On the other hand, Chisholm et al. (2017) has argued, using COS spectroscopy of low redshift galaxies, that the same trend (albeit, at a different redshift) can be explained by changing column densities and optically thin LIS lines. Regardless of the origin, Figure 11 tests for a relation by comparing  $f_{esc}^{Ly\alpha}$  and  $f_{esc}^{Mg II}$  to the equivalent widths of four LIS lines: Si II  $\lambda 1190$ ,  $\lambda 1193$ ,  $\lambda 1260$ , and C II  $\lambda 1334$ . This analysis shows that, while the higher escape fraction objects are among those with weaker LIS absorption, any trend is only tentative. We calculated the Pearson coefficient for a correlation between  $f_{esc}^{Mg II}$  with the equivalent width of each LIS line, finding that the probability of the null hypothesis ranges from a few to 30%. We note that small samples, covering a small dynamic range cannot always detect a correlation in these quantities (Henry et al. 2015). We also do not detect a correlation between  $f_{esc}^{Ly\alpha}$  and the equivalent widths of the LIS lines in Figure 11, even though it has been seen in larger samples (using  $W_{Ly\alpha}$  as a proxy for  $f_{esc}^{Ly\alpha}$ ; e.g. Shapley et al. 2003; Chisholm et al. 2017). Therefore, the large scatter in Figure 11 is not surprising; more observations are needed to determine how  $f_{esc}^{Mg II}$  varies with the equivalent widths of the LIS lines.

Finally, if Ly $\alpha$  and Mg II profiles are shaped by radiation transport in the same scattering gas, we might expect some kinematic measures from the line profiles to correlate. This idea is supported the fact that our observations were able to resolve double-peaked Mg II profiles for 1244+0216, which has a relatively large Ly $\alpha$  peak separation for the Green Peas in this sample. Since we expect broader, more redshifted emission when the column densities of gas are higher, we checked for a relation between the Mg II peak velocities, and the velocities of the red and blue Ly $\alpha$  peaks. Similarly, we compared the FWHM of the Ly $\alpha$  and Mg II lines. In these cases, we see no evidence of a correlation. It is possible, as with the (lack of) correlation between the  $f_{esc}^{Mg II}$  and the

equivalent width of the LIS lines, that a larger sample and more dynamic range is needed.

## 5. SUMMARY AND IMPLICATIONS

We have shown that Mg II appears in emission instead of absorption in Green Pea galaxies. Previous studies that aim to constrain outflows from this spectral feature have noted emission in some cases (Erb et al. 2012; Martin et al. 2012), but the origin of this emission has been unclear. Nevertheless, we showed that Cloudy models predict appreciable emission from H II regions (previously noted by Erb et al. 2012 and Jaskot & Ravindranath 2016) that can easily explain the spectra of these Green Pea galaxies.

Because we have a wealth of other information about the Green Peas, we have characterized their Mg II emission to better understand its use as a diagnostic. Since Mg II photons are resonantly trapped like Ly $\alpha$ , it is not surprising that we detect some effects of radiation transport on the lines. We show that photoionization models can be used to predict the intrinsic Mg II line fluxes, thereby allowing measurement of Mg II escape fractions (analogous to Ly $\alpha$ ). These escape fractions vary between 0 and 95%, and are often lower than the prediction for simple dust extinction without resonant scattering. We show that lower escape fractions are tentatively associated with Mg II lines that are broader and more redshifted, which can be an indication of higher column densities of scattering gas. In particular, the line profiles of the Green Pea 1244+0216 are remarkable in the sense that they are double peaked and substantially broader than H $\beta$ . This observation makes sense qualitatively, since 1244+0216 is among the objects with the broadest Ly $\alpha$  peak separations and lowest Mg II and Ly $\alpha$  escape fractions.

At the same time, however, the effects of radiation transport that we observe are substantially weaker than we see for Ly $\alpha$ . First, the line fluxes remain close to their intrinsic ratio. Likewise, the escape fractions of the  $\lambda 2796$  and  $\lambda 2803$  are mostly consistent within the er-

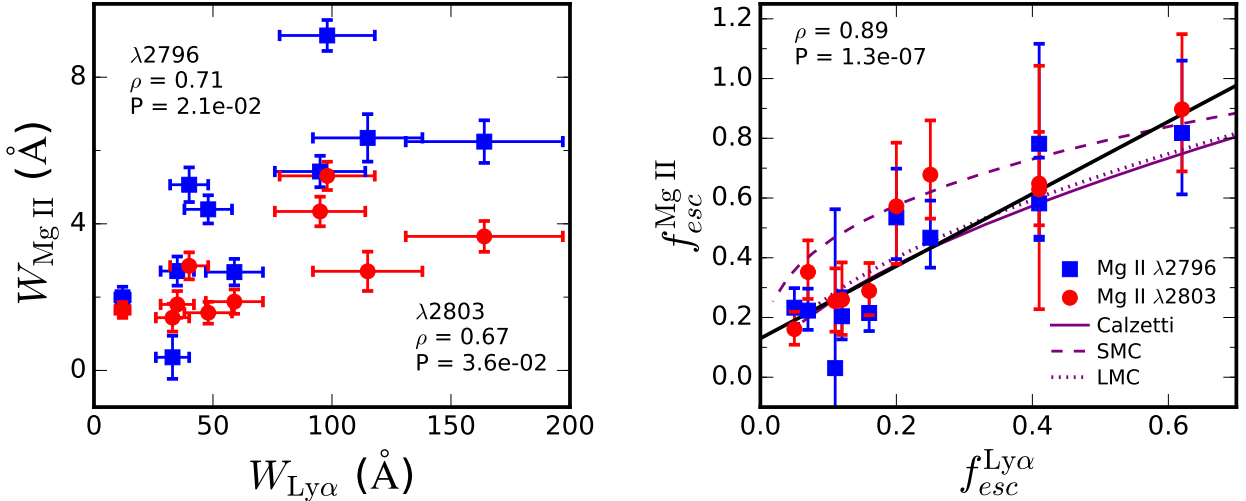


**Figure 10.** The equivalent widths and escape fractions correlate for Ly $\alpha$  and Mg II. The Pearson correlation coefficient and probability of the null hypothesis are shown in each panel, for the Mg II lines separately in the equivalent width panel (left), or for combined set of measurements in the escape fraction panel (right). The black line shows a linear fit to the relation, given by Equation 5. The purple curves show the expectation from dust extinction *without* resonant scattering. We note that neither the Ly $\alpha$  or Mg II escape fractions are corrected for any extended emission that may fall outside the spectroscopic apertures.

rors (except for one case), despite the fact that the blue line has twice the oscillator strength (scattering optical depth) of the red line. Finally, we do not see any evidence of scattered Mg II emission extending beyond the stellar continuum, in contrast to cases seen by Rubin et al. (2011) and Martin et al. (2013). We acknowledge, however, that this constraint is not particularly strong. Yang et al. (2017b) measure the spatial extent of the Ly $\alpha$  and UV continuum in 9/10 of the Green Peas in the present sample, and while the Ly $\alpha$  is 1.3 to 1.9 times more extended than the continuum, the Ly $\alpha$  sizes are still sub-arcsecond. Since the size of the Mg II should not exceed Ly $\alpha$ , we conclude that our ground-based observations would be unlikely to detect extended Mg II. Overall, we conclude that in comparison to Ly $\alpha$ , weaker radiation transport effects on Mg II are sensible, since the column density of Mg II is orders of magnitude lower than that of H I. Still, we are puzzled that resonant scattering in a dusty ISM produces Ly $\alpha$  and Mg II escape fractions that are of the same order of magnitude. Since Ly $\alpha$  photons scatter much more than Mg II photons, we might expect the Ly $\alpha$  escape fractions to be substantially lower than Mg II escape fractions.

Intriguingly, the Mg II escape fractions show a tight correlation with the Ly $\alpha$  escape fraction. This relation suggests that the same gas that scatters Ly $\alpha$  photons and sets their escape is also regulating the Mg II output. In some ways, this result is not surprising: Mg II is a low ionization line that serves as a proxy for H I. However, in other ways, it is noteworthy. In spectra of high-redshift galaxies, the ISM metal absorption lines have been postulated to trace dense clumps in an outflow (Shapley et al. 2003), possibly different from the pervasive H I component that is indicated by Lyman series absorption lines (Trainor et al. 2016; Reddy et al. 2016). If the Green Peas are like high-redshift galaxies, it is not obvious that the dense gas which is most effective at scattering Mg II photons is co-spatial with large H I reservoir that scatters Ly $\alpha$  photons (Henry et al. 2015). Nevertheless, Mg II

appears to serve as an effective tracer of H I since the correlation between the escape fractions is surprisingly tight. More detailed radiation transport modeling will be required to understand the properties of outflows and the ISM/CGM that can produce this relation.

### 5.1. Implications for the Epoch of Reionization

The close correspondence between Ly $\alpha$  and Mg II could have great utility in the epoch of reionization, where observations of Ly $\alpha$  are difficult or impossible. Two diagnostics stand out. First, Mg II may be useful for predicting the Ly $\alpha$  that emerges from the ISM, before it is diffused and rendered unobservable by a partially neutral IGM. Significant efforts have been made to measure the neutral hydrogen fraction in the IGM from weakened or absent Ly $\alpha$  emission at  $z > 6$  (e.g., Mason et al. 2017, and references therein). However, it is unclear how Ly $\alpha$  would evolve over these redshifts in a completely ionized IGM; hence, the high-redshift Ly $\alpha$  deficit is ill-defined, and inferred IGM neutral fractions are uncertain. Importantly, Mg II emission from galaxies would not be impacted by a neutral IGM in the same way. We can estimate the optical depth for scattering Mg II photons in the IGM at early times, using metallicity measurements from Damped Ly $\alpha$  Absorber (DLA) observations. Observations have indicated  $[\text{Mg}/\text{H}] \sim -2.0$  at  $z \sim 5$ , with probably declines to higher redshifts (Rafelski et al. 2014). Taking this value as an upper limit, and conservatively assuming that all Mg in a neutral IGM would be in Mg II, we estimate that  $\text{Mg II}/\text{H} \lesssim 10^{-6.4}$ , where the solar abundance scale as been adopted (Grevesse et al. 2010). Since the column density where Ly $\alpha$  becomes optically thick at line center ( $\tau_{\text{Ly}\alpha}^{\text{IGM}} = 1$ ) is around  $3 \times 10^{13} \text{ cm}^{-2}$  (the precise quantity depends on the Doppler parameter; Verhamme et al. 2006), the column density of Mg II is at most  $10^7 \text{ cm}^{-2}$  when Ly $\alpha$  photons start to see the effects of a neutral IGM. Hence, the optical depth of Mg II at line center will be  $\tau_{\text{MgII}}^{\text{IGM}} \sim 10^{-6}$ , completely

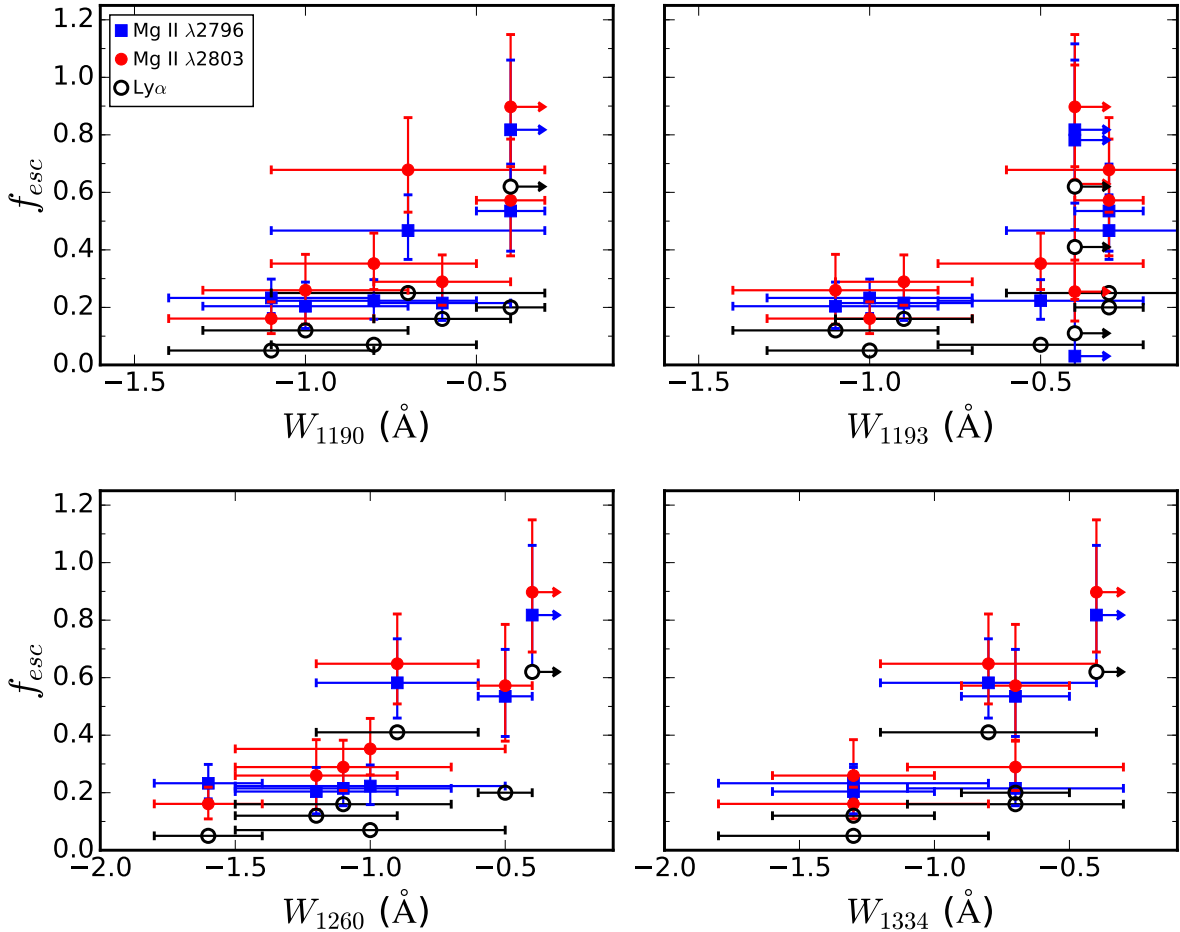


**Figure 11.** The Mg II and Ly $\alpha$  escape fractions are compared to the equivalent widths of the LIS lines of Si II  $\lambda\lambda$ 1190, 1193,  $\lambda$ 1260 and C II  $\lambda$ 1334, measured from the FUV COS spectra. Previous studies have detected a relation between equivalent widths of these lines and the Ly $\alpha$  escape fraction or equivalent width (Shapley et al. 2003; Jones et al. 2012, 2013; Chisholm et al. 2017). While the Mg II lines are corrected for stellar absorption following Guseva et al. (2013), the corrections to the FUV lines are not applied because we showed they are small (see Henry et al. 2015).

optically thin and unaffected by the neutral IGM. Critically, this means that we could use Mg II to predict the Ly $\alpha$  that emerges from the ISM and CGM, before it is impacted by the neutral IGM. Comparison with observations could then allow more robust measurements of the Ly $\alpha$  deficit and IGM neutral fraction at very high-redshifts.

The second reionization-epoch utility for Mg II is as a diagnostic for Lyman Continuum (LyC) leakage. High Ly $\alpha$  escape fractions have been associated with narrowly spaced Ly $\alpha$  peaks, low H I column densities, and direct detection of escaping LyC (Henry et al. 2015; Verhamme et al. 2015, 2017; Izotov et al. 2016a,b, 2017, 2018). Because Ly $\alpha$  and Mg II escape appear to be governed by radiation transport in the same gas, we postulate that Mg II may also be used to predict LyC emission. This hypothesis is supported by the detection of Mg II in the SDSS spectrum of the LyC emitter, J1154+2443 (Izotov et al. 2018), although a higher signal-to-noise spectrum

will be required for a detailed comparison to the sources presented here. Ultimately, Mg II may be particularly useful at  $z > 6 - 7$ , where Ly $\alpha$  becomes unobservable due to the neutral IGM. With NIRSpect on JWST, these observations will soon be possible. We can estimate the required exposure time to detect Mg II from a 26.5th magnitude galaxy with  $W = 7 \text{ \AA}$  (rest) on each of the Mg II lines. For this calculation, we simulate a 1D spectrum, assuming NIRSpect’s G235H disperser with varying levels of noise, and measure the significance of the simulated line. We find that a continuum signal-to-noise of 1.5 per pixel is required to detect the Mg II lines with a signal-to-noise of 5. Using the JWST Exposure Time Calculator<sup>10</sup>, we find that 48 hours of observation should meet this goal. While expensive, detections of Mg II in the reionization epoch should be possible as part of a comprehensive, deep spectroscopic survey. Clearly, before we can confidently use Mg II as a diagnostic for

<sup>10</sup> <https://jwst.etc.stsci.edu/>

reionization, more work will be needed to characterize its emission and relationship with Ly $\alpha$  in an ionized IGM. Nevertheless, the trends that we have presented here appear promising.

### 5.2. Implications for the properties of galaxies and outflows

We have shown that the Mg II feature originates from nebular line photons, which resonantly scatter to escape galaxies, analogous to Ly $\alpha$ . This finding implies that studies which aim to use Mg II for constraining outflows *must* account for the emitted line photons. Models which seek to reproduce the Mg II line profiles with only scattered continuum photons should struggle to reproduce observations (Prochaska et al. 2011; Scarlata & Panagia 2015; Zhu et al. 2015; Bordoloi et al. 2016, Carr et al., submitted). Indeed, in Erb et al. (2012), significant differences between Mg II and Fe II line profiles were attributed to a contribution from nebular Mg II emission. Our Green Pea observations confirm this interpretation. In short, when Mg II is used, measurements of galaxy outflow velocities, column densities, and mass-loss rates will require more sophisticated modeling than has yet been attempted for this spectral feature. Fortunately, these radiation transport models have already been developed for interpreting Ly $\alpha$  emission (Dijkstra et al. 2006; Behrens et al. 2014; Zheng & Wallace 2014; Verhamme et al. 2006, 2008, 2015).

The observations that we report here provide further context for interpreting higher redshift observations. Notably, Finley et al. (2017) report Mg II emission is common among low mass galaxies ( $M < 10^9 M_{\odot}$ ) at  $z \sim 1$ , but less common at high masses. Within this sample, the lower mass galaxies will have relatively lower metallicities than the high mass galaxies, so they should also have correspondingly higher O32. Hence, following our photoionization models, we expect that the intrinsic Mg II/[O III] ratio (and possibly the intrinsic Mg II flux), weakens at lower masses. Therefore, the strongest Mg II emitters in Finley et al. (2017) probably have high Mg II (and Ly $\alpha$ ) escape fractions. These trends among the Green Peas and  $z \sim 1$  galaxies could be an indication that a highly ionized ISM (high O32) results in low column densities of neutral and low-ionization state gas, allowing high Mg II and Ly $\alpha$  escape fractions. Additionally, given our understanding of Mg II escape, it makes sense that the  $z \sim 1$  galaxies with Mg II emission tend not to have fluorescent Fe II\* emission (Finley et al. 2017). While nebular Mg II emission favors ISM with low column densities of gas, fluorescent Fe II\* is the opposite. Non-negligible absorption in resonant Fe II, from higher column densities of gas, is required to produce Fe II\* emission. The opposite trend—stronger Fe II\* emission when Mg II is strong—reported by Erb et al. (2012) is somewhat puzzling. However, these results are based on composite spectra, and aperture losses on the scattered emission would also tend to correlate the strength of these emission features.

Our analysis of Mg II also points to an important warning about the use of resonant lines for constraining the physical conditions in H II regions. For example, observations of nebular C IV have been reported from galaxies at both high and low-redshifts (Stark et al. 2014; Mainali et al. 2017; Schmidt et al. 2017; Senchyna et al. 2017), and used to quantify the number of hard ionizing pho-

tons from young stars. However, by analogy with Mg II, we infer that escape fractions may be anywhere between zero and one. Indeed, at low impact parameter in the CGM of low-redshift galaxies, Bordoloi et al. (2014) find C IV column densities around  $N = 10^{14}$ , which implies C IV optical depth at line center of  $\tau \gtrsim 1 - 2$ . Hence, we expect resonant-line radiation transport to be significant; this may explain the apparent redshifting of C IV in some low-redshift galaxies with high-signal to noise UV spectra and known systemic redshifts (Senchyna et al. 2017). Although C IV is commonly used as a diagnostic for the physical conditions in HII regions (e.g. Stark et al. 2014; Gutkin et al. 2016; Feltre et al. 2016) we conclude that this approach is probably unreliable, even when the C IV stellar wind feature can be confidently subtracted. Despite this complication, the resonant nature of C IV could prove useful for understanding the CGM, similar to Ly $\alpha$  and Mg II. It would be curious to test whether C IV emission and escape<sup>11</sup> correlate with Ly $\alpha$  as Mg II does. The C IV traces different gas than Mg II and Ly $\alpha$ , so we would not necessarily expect the same close relationship that we see between Mg II and Ly $\alpha$ . Still, any correlation, or lack thereof, could place constraints on the multi-phase nature of the ISM and CGM.

### 5.3. Future Work

Finally, we conclude that these observations mark an important first step in the characterization of Mg II and its relation with Ly $\alpha$ . We have shown that simultaneous observations of multiple resonance lines probing neutral and low-ionization state gas can give qualitatively consistent results. We provide evidence that Mg II may be able to predict the Ly $\alpha$  that emerges from galaxies, before it is impacted by a neutral IGM at high redshifts. As a consequence of its close correlation with Ly $\alpha$ , Mg II may also serve as a useful LyC diagnostic at high redshifts. Overall, larger samples at all redshifts will be useful for strengthening our conclusions about the physical processes that allow Ly $\alpha$ , Mg II, and LyC escape. Indeed, at  $z \gtrsim 3$ , Mg II and the full rest-frame optical spectrum can be observed with JWST/NIRSpec, and ground based-data can cover Ly $\alpha$  at  $z < 6$ . Hence, the data to test these theories at high redshifts will soon be available. In the mean time, simultaneous radiation transport modeling of the Ly $\alpha$  and Mg II lines will be an intriguing test of models for outflows and the CGM.

The authors thank the anonymous referee for insightful comments, which improved this work. AH thanks Marc Rafelski, Nicolas Bouché, Tim Heckman and Molly Peeples for useful suggestions, Anne Jaskot for help with Cloudy models, and James White for reducing the Keck/ESI spectra. The authors also wish to thank the Lorentz Center for facilitating collaboration during the “Characterizing Galaxies with Spectroscopy with a view for JWST” workshop. This work was supported in part by HST GO 13654.

## REFERENCES

Angel, J. R. P., Hilliard, R. L., & Weymann, R. J. 1979, *The MMT and the Future of Ground-Based Astronomy*, 385, 87

<sup>11</sup> We acknowledge that photoionization modeling to predict intrinsic C IV may not be as straightforward as with Mg II.

- Behrens, C., Dijkstra, M., Neimeyer, J. C. 2014, *A&A*, 563, 77
- Berg, D. A., Skillman, E. D., Croxall, K. V., et al. 2015, *ApJ*, 806, 16
- Boeshaar, G. O., Harvel, C. A., Mallama, A. D., et al. 1982, NASA Conference Publication, 2238, 374
- Bordoloi, R., Tumlinson, J., Werk, J., et al. 2014, *ApJ*, 796, 136
- Bordoloi, R., Rigby, J. R., Tumlinson, J., et al. 2016, *MNRAS*, 458, 1891
- Calzetti, D. Armus, L., Bohlin, R. C., et al. 2000, *ApJ*, 533, 682
- Cardamone, C., Schawinski, K., Sarzi, M., et al. 2009, *MNRAS*, 399, 1191
- Cardelli, J. A., Clayton, G. C., Mathis, J. S. 1989, *ApJ*, 345, 245
- Chisholm, J., Orlitová, Schaerer, D., et al. 2017, *A&A*, 605, 67
- Coil, A. L., Weiner, B. J., Holz, D. E., et al. 2011, *ApJ*, 743, 46
- Davies, B., Kudritzki, R.-P., Lardo, C., et al., arXiv:1708.08948
- De Cia, A., Ledoux, C., Mattson, L., et al. 2016, *A&A*, 596, 97
- Dijkstra, M. Haiman, Z., & Spaans, M. 2006, *ApJ*, 649, 37
- Dopita, M. A., & Sutherland, R. S. 2003, *Astrophysics of the diffuse universe*, Berlin, New York: Springer, 2003. *Astronomy and astrophysics library*, ISBN 3540433627,
- Erb, D. K., Pettini, M., Shapley, A. E., et al. 2010, *ApJ*, 719, 1168
- Erb, D. K., Quider, A. M., Henry, A. L., & Martin, C. L. 2012, *ApJ*, 759, 26
- Eldridge, J. J., & Stanway, E. R. 2009, *MNRAS*, 419, 479
- Eldridge, J. J., Stanway, E. R., Xiao, L., et al. 2017, *PASA*, 34, e058
- Feltre, A., Charlot, S., Gutkin, J. 2016, *MNRAS*, 456, 3354
- Ferland, G. J., Chatzikos, M., Guzmán, F., et al., arXiv:1705.10877
- Filippenko, A. V. 1982, *PASP*, 94, 715
- Finley, H., Bouché, N., Contini, T., et al. 2017, *A&A*, in press, arXiv:1710.09195
- Finkelstein, S. L., Rhoads, J. E., Malhotra, S., Pirzkal, N., & Wang, J. X. 2007, *ApJ*, 660, 1023
- Fitzpatrick, E. L. 1999, *PASP*, 111, 63
- Gordon, K. D., Clayton, G. C., Misselt, K. A., Landolt, A. U., & Wolff, M. J. 2003, *ApJ*, 594, 279
- Garnett, D. R., 1992, *AJ*, 103, 1330
- Gawiser, E. J., Francke, H., Lai, K., et al. 2007, *ApJ*, 671, 278
- Gehrels, N. 1986, *ApJ*, 303, 336
- Grevesse, N., Asplund, M., Sauval, A. J., & Scott, P. 2010, *Ap & SS*, 328, 179
- Guseva, N. G., Izotov, Y. I., Fricke, K. J., & Henkel, C. 2013, *A&A*, 555, 90
- Gutkin, J., Charot, S., Bruzual, G. 2016, *MNRAS*, 462, 1757
- Hanuschik, R. W. 2003, *A&A*, 407, 1157
- Hayes, M., Östlin, G., Duval, F., et al. 2014, *ApJ*, 782, 6
- Henry, A., Scarlata, C., Erb, D., & Martin, C. 2015, *ApJ*, 809, 19
- Izotov, Y. I., Guseva, N. G., Thuan, T. X. 2011, *ApJ*, 728, 161
- Izotov, Y., Orlitová, I., Schaerer, D., et al. 2016a, *Nature*, 529, 178
- Izotov, Y., Schaerer, D., Thuan, T. X., et al. 2016b, *MNRAS*, 461, 3683
- Izotov, Y., Schaerer, D., Worseck, G., et al. 2017, arXiv:1711.11449
- Izotov, Y., Schaerer, D., Worseck, G. 2018, *MNRAS*, 474, 4514
- Jaskot, A. E., & Ravindranath, S. 2016, *ApJ*, 833, 136
- Jones, T., Stark, D. P., Ellis, R. 2012, *ApJ*, 751, 51
- Jones, T. A., Ellis, R. S., Schenker, M. A., Stark, D. P. 2013, *ApJ*, 779, 52
- Karman, W., Grillo, C., Balestra, I. 2016, *A&A*, 585, 27
- Kornei, K. A., Shapley, A. E., Martin, C. L., et al. 2012, *ApJ*, 758, 135
- Kornei, K. A., Shapley, A. E., Martin, C. L., et al. 2013, *ApJ*, 774, 50
- Kroupa, P. 2001, *MNRAS*, 322, 231
- Leclercq, F., Bacon, R., Wistotzki, L. et al. 2017, *A&A*, in press, arXiv:1710.10271
- Leitherer, C., Schaerer, D., Goldader, J., et al. 1999, *ApJS*, 123, 3
- Leitherer, C., Ekström, S., Meynet, G., et al. 2014, *ApJS*, 212, 14
- Mainali, R., Kollmeier, J. A., Stark, D. P., et al. 2017, *ApJ*, 836, 14L
- Martin, C. L. & Bouché, N. 2009, *ApJ*, 703, 1394
- Martin, C. L., Shapley, A. E., Coil, A. L., et al. 2012, *ApJ*, 760, 127
- Martin, C. L., Shapley, A. E., Coil, A. L., et al. 2013, *ApJ*, 770, 41
- Mason, C., Treu, T., Dijkstra, M. et al. 2017, arXiv:1709.5356
- Moustakas, J., & Kennicutt, R. C. 2006, *ApJ*, 164, 81
- Prochaska, J. X., Kasen, D., & Rubin, K. 2011, *ApJ*, 734, 24
- Rafelski, M., Neeleman, M., Fumagalli, M., Wolfe, A. M., & Prochaska, J. X. 2014, *ApJ*, 782, 29L
- Reddy, N. A., Steidel, C. C., Pettini, M., Bogosavljević, M., Shapley, A. 2016, *ApJ*, 828, 108
- Rigby, J. R., Bayliss, M. B., Gladders, M. D., et al. 2014, *ApJ*, 790, 44
- Rubin, K. H. R., Weiner, B. J., Koo, D. C., et al. 2010, *ApJ*, 719, 1503
- Rubin, K. H. R., Prochaska, J. X., Ménard, B., et al. 2011, *ApJ*, 728, 55
- Scarlata, C. Colbert, J., Teplitz, H. I., et al. 2009, *ApJ*, 704, 98L
- Scarlata, C. & Panagia, N. 2015, *ApJ*, 801, 43
- Schlafly, E. F., & Finkbeiner, D. P. 2011, *ApJ*, 737, 103
- Schmidt, K. B., Huang, K.-H., Treu, T., et al. 2017, *ApJ*, 839, 17
- Senchyna, P., Stark, D. P., Vidal-García, A., et al. 2017, *MNRAS*, 472, 2608
- Shapley, A. E. Steidel, C. C., Pettini, M., & Adelberger, K. L. 2003, *ApJ*, 588, 65
- Stark, D. P., Richard, J. P., Siana, B., et al. 2014, *MNRAS*, 445, 3200
- Steidel, C. C., Strom, A. L., Pettini, M., et al. 2016, *ApJ*, 826, 159
- Tang, Y., Giavaolsco, M., Guo, Y., & Kurk, J. 2014, *ApJ*, 793, 92
- Trainor, R. F. Strom, A. L., Steidel, C. C., Rudie, G. C. *ApJ*, 2016, 832, 171
- Verhamme, A., Schaerer, D., & Maselli, A., *A&A*, 460, 397
- Verhamme, A., Schaerer, D., Atek, J., Tapken, C. 2008, *A&A*, 491, 89
- Verhamme, A., Orlitová, I., Schaerer, D., & Hayes, M. 2015, *A&A*, 578, 7
- Verhamme, A., Orlitová, I., Schaerer, D., et al. 2017, *A&A*, 597, 13
- Weiner, B. J., Coil, A. L., Prochaska, J. X., et al. 2009, *ApJ*, 692, 187
- Wisotzki, L., Bacon, R., Blaizot, J. et al. 2016, *A&A*, 587, 98
- Yang, H., Malhotra, S., Gronke, M., et al. 2017a, *ApJ*, 844, 171
- Yang, H., Malhotra, S., Rhoads, J., et al. 2017b, *ApJ*, 838, 4
- Zahid, H. J., Kudritzki, R. P., Conroy, C. Andrews, B., Ho, I.-T. 2017, arXiv:1708.07107
- Zheng, Z., & Wallace, J. 2014, *ApJ*, 794, 116
- Zhu, G. B., Comparat, J., Keib, J.-P., et al. 2015, *ApJ*, 815, 48

**Table 2**  
Comparison Data for the Green Peas

ID	$E(B-V)_{gas}$	O32	$F([\text{OIII}] \ 5007)$ ( $10^{-14} \text{ erg s}^{-1} \text{ cm}^{-2}$ )	$12 + \log(\text{O}/\text{H})$	$F(\text{Ly}\alpha)$ ( $10^{-14} \text{ erg s}^{-1} \text{ cm}^{-2}$ )	$f_{esc}^{\text{Ly}\alpha}$	$W_{\text{Ly}\alpha}$ ( $\text{\AA}$ )	$v_{blue}^{peak}$ ( $\text{km s}^{-1}$ )	$v_{red}^{peak}$ ( $\text{km s}^{-1}$ )
(1)	(2)	(3)	(4)	(5)	(6)	(7)	(8)	(9)	(10)
0911+1831	0.17	0.26	1.57	7.90	$3.3 \pm 0.1$	0.16	$59 \pm 12$	-280	90
0926+4427	0.10	0.51	4.60	7.95	$6.0 \pm 0.3$	0.20	$40 \pm 8$	-250	160
1054+5238	0.08	0.40	3.29	8.22	$1.7 \pm 0.2$	0.07	$12 \pm 3$	-250	160
1137+3524	0.06	0.45	5.24	8.14	$3.8 \pm 0.2$	0.12	$35 \pm 7$	-400	150
1219+1526	0.00	1.02	5.71	7.86	$13.7 \pm 0.2$	0.62	$164 \pm 33$	-100	140
1244+0216	0.07	0.56	5.74	8.12	$2.0 \pm 0.1$	0.07	$48 \pm 10$	-280	250
1249+1234	0.07	0.55	2.52	8.10	$5.4 \pm 0.1$	0.41	$98 \pm 20$	...	70
1424+4217	0.04	0.79	7.92	7.99	$8.5 \pm 0.2$	0.25	$95 \pm 19$	-150	230
1440+4619	0.16	0.25	2.05	8.17	$2.3 \pm 0.2$	0.11	$33 \pm 7$	-470	70
1442-0209	0.12	0.83	2.05	7.93	$5.1 \pm 0.2$	0.41	$115 \pm 23$	-230	100

**Note.** — Comparison data for the Green Peas are drawn from SDSS and HST/COS spectroscopy.  $\text{Ly}\alpha$  measurements are either taken from Henry et al. (2015), or, in the case of 1440+4619 and 1442-0209 measured in the same way. Column descriptions: (1) object ID; (2) nebular dust extinction, calculated from  $\text{H}\alpha/\text{H}\beta$ , using the Calzetti et al. (2000) extinction curve; (3)  $\text{O32} \equiv \log([\text{O III}] \ \lambda 5007 / [\text{O II}] \ \lambda 3727)$ , corrected for dust; (4)  $[\text{O III}] \ \lambda 5007$  flux, corrected for dust; (5) gas-phase metallicity, calculated following Berg et al. (2015). The values given here differ slightly from those in Henry et al. (2015), where they were instead taken from Izotov et al. (2011); (6) The  $\text{Ly}\alpha$  flux measured from the COS spectra, corrected for Milky Way foreground attenuation using Schlafly & Finkbeiner 2011 extinction measurements and the Fitzpatrick 1999 extinction law; (7) the  $\text{Ly}\alpha$  escape fraction; (8) the rest-frame  $\text{Ly}\alpha$  equivalent width; (9) the velocity marking the blue peak of the  $\text{Ly}\alpha$  line profile; (10) the velocity marking the red peak of the  $\text{Ly}\alpha$  line profile.

**Table 3**  
Mg II Measurements from Green Peas

ID	$W_{2796}$	$W_{2803}$	$F_{2796}$	$F_{2803}$	$v_{2796}$	$v_{2803}$	FWHM <sub>2796</sub>	FWHM <sub>2803</sub>	$f_{esc}$ (2796)	$f_{esc}$ (2803)
(1)	(2)	(3)	(4)	(5)	(6)	(7)	(8)	(9)	(10)	(11)
	(Å)	(Å)	( $10^{-16}$ erg s $^{-1}$ cm $^{-2}$ )	( $10^{-16}$ erg s $^{-1}$ cm $^{-2}$ )	(km s $^{-1}$ )	(km s $^{-1}$ )	(km s $^{-1}$ )	(km s $^{-1}$ )		
0911+1831	2.9 ± 0.4	1.9 ± 0.3	5.5 ± 1.0	3.7 ± 0.8	67 ± 12	94 ± 28	122 ± 59	121 ± 68	0.21 $^{+0.07}_{-0.06}$	0.29 $^{+0.08}_{-0.08}$
0926+4427	5.1 ± 0.5	2.9 ± 0.5	21.7 ± 3.4	12.2 ± 3.3	91 ± 10	65 ± 32	208 ± 46	93 ± 69	0.53 $^{+0.16}_{-0.13}$	0.57 $^{+0.21}_{-0.19}$
1054+5238	3.0 ± 0.3	1.6 ± 0.2	8.4 ± 1.7	6.9 ± 1.1	113 ± 9	122 ± 22	193 ± 38	159 ± 46	0.23 $^{+0.07}_{-0.05}$	0.36 $^{+0.11}_{-0.09}$
1137+3524	2.7 ± 0.4	1.8 ± 0.4	10.8 ± 4.1	7.2 ± 2.9	123 ± 9	138 ± 44	< 90	91 ± 59	0.20 $^{+0.07}_{-0.07}$	0.26 $^{+0.11}_{-0.08}$
1219+1526	6.2 ± 0.5	3.7 ± 0.3	14.1 ± 2.0	8.6 ± 0.9	34 ± 7	86 ± 17	132 ± 45	90 ± 40	0.80 $^{+0.24}_{-0.21}$	0.90 $^{+0.25}_{-0.22}$
1244+0216	4.4 ± 0.4	1.6 ± 0.3	10.6 ± 1.2	3.8 ± 0.9	72 ± 8	55 ± 38	327 ± 44	195 ± 119	0.24 $^{+0.07}_{-0.04}$	0.16 $^{+0.06}_{-0.05}$
1249+1234	9.1 ± 0.4	5.3 ± 0.4	12.0 ± 0.5	7.1 ± 0.5	44 ± 4	60 ± 23	122 ± 31	121 ± 38	0.58 $^{+0.16}_{-0.13}$	0.65 $^{+0.17}_{-0.13}$
1424+4217	5.4 ± 0.3	4.3 ± 0.3	18.1 ± 1.1	14.1 ± 0.9	29 ± 5	50 ± 13	92 ± 41	133 ± 52	0.46 $^{+0.13}_{-0.10}$	0.68 $^{+0.18}_{-0.15}$
1440+4619	0.4 ± 0.5	1.4 ± 0.3	1.0 $^{+17.2}_-1.0}$	4.3 ± 1.4	87 ± 21	24 ± 42	311 ± 110	151 ± 148	0.03 $^{+0.54}_{-0.03}$	0.25 $^{+0.11}_{-0.11}$
1442-0209	6.3 ± 0.7	2.7 ± 0.6	7.2 ± 2.5	3.1 ± 2.0	24 ± 14	9 ± 25	153 ± 37	116 ± 44	0.78 $^{+0.34}_{-0.30}$	0.61 $^{+0.42}_{-0.40}$

**Note.** — Measurements of the Mg II emission lines from our MMT spectra. Column descriptions: (1) object ID; (2-3) rest frame equivalent widths for the  $\lambda 2796$  and  $\lambda 2803$  lines. A stellar absorption correction of 0.3 Å is added. The  $\lambda 2796$  line is measured including any blueshifted absorption, hence, 1440+4619 has  $W_{2796} \sim 0$  Å before the stellar absorption correction. (3-4) line fluxes are corrected for stellar absorption, slit-losses (see §2), and the Milky Way foreground attenuation. The latter correction uses the Schlafly & Finkbeiner (2011) extinction measurements and the Fitzpatrick (1999) extinction law. (5-6) velocities marking the peaks of the lines. (7-8) FWHM of the lines, corrected for instrumental resolution (9-10) Mg II escape fractions, calculated by correcting for stellar absorption, slit losses and Milky Way extinction, but not corrected for internal dust extinction. Errors on the Mg II escape fraction include the measurement uncertainty on the observed flux and a 0.1 dex uncertainty on the predicted intrinsic Mg II flux.

<sup>a</sup> The measured equivalent width on this line is small compared to the stellar absorption correction, so the flux is multiplied by a factor of 6.2. Prior to this correction, we measure  $F_{2796} = 0.16_{-0.16}^{+2.8} \times 10^{-16}$  erg s $^{-1}$  cm $^{-2}$ .